

A Self-Consistent Open Boundary Condition for Fully Kinetic Plasma Thruster Plume Simulations

Revathi Jambunathan^{ID} and Deborah A. Levin

Abstract—A new, charge-conserving, energy-based, open boundary condition (BC) is developed and used to perform steady-state plasma plume simulations. This BC prevents the numerical instability, which is typically observed for kinetic simulations that employ the traditional outflow boundary, and thus allows the fully kinetic plume simulations to reach a steady-state with finite computational domain sizes. In addition to modeling a plume with colocated electron-ion sources, the BC is also applied to separated electron-ion sources which model realistic thrusters with a separate external neutralizer configuration without assuming quasi-neutrality. Domain-independence simulations performed with the new open boundary construct showed that the electric field obtained from small and large domain sizes agree within 2%. For the separated electron-ion plume, the minimum domain size required to obtain convergence is such that it must accommodate the plume until the charge density decreases by an order of magnitude. The computational cost of the electrostatic particle-in-cell simulation was found to decrease by a factor of four when the domain size was decreased by one-half.

Index Terms—Ion thruster plasma plume, neutralization, open boundary condition (BC), particle-in-cell (PIC).

I. INTRODUCTION

ELECTRIC propulsion devices emit a high-velocity ion plume to generate thrust required for the station-keeping of satellites. A hollow cathode is mounted externally on the spacecraft to neutralize the charge within the thruster exhaust plume [1]. Without an external neutralizer, the thruster plumes would acquire a higher positive charge compared to the spacecraft surface and the solar panel, which, in turn, would decelerate the plume ions causing a decrease in the thrust efficiency. In the case of higher potential differences between the plume and the backflow environment, the plume ions may stream backward and impinge upon the solar panels, resulting in the sputtering and deterioration of the performance and the lifetime of the satellite [2]. Thus, predicting the

Manuscript received April 25, 2019; revised August 5, 2019 and November 4, 2019; accepted December 17, 2019. Date of publication February 7, 2020; date of current version March 10, 2020. This work was supported in part by AFOSR under Grant AF FA9550-16-1-0193, in part by the National Science Foundation through the Blue Waters Sustained-Petascale Computing Project under Grant OCI-0725070 and Grant ACI-1238993, and in part by the state of Illinois. The review of this article was arranged by Senior Editor F. Taccogna. (*Corresponding author: Revathi Jambunathan.*)

The authors are with the Department of Aerospace Engineering, University of Illinois at Urbana-Champaign, Urbana, IL 61801 USA (e-mail: rjambunathan@illinois.edu).

Color versions of one or more of the figures in this article are available online at <http://ieeexplore.ieee.org>.

Digital Object Identifier 10.1109/TPS.2020.2968887

plume characteristics and its interaction with the electrons as well as solar panels are a prerequisite to optimize the design and configuration of the thruster devices on the satellites. However, the evolution of electron kinetics and its effect on the plume expansion are still not well understood. Direct plume measurements of plume kinetic characteristics are challenging, and a more detailed analysis can be obtained by performing simulations of the plume evolution.

Ion thruster plume densities are on the order of $10^{15}/\text{m}^3$ [1], [3], with negligible collision frequencies among the charged ion and electron species, and therefore a fully kinetic numerical approach is required to capture the electron kinetics and provide a detailed insight into the neutralization process. Particle-in-cell (PIC) is a well-established kinetic approach used to model low-density plasma systems [4]. The PIC approach has been used for a wide variety of applications, such as modeling of electromagnetic solar-wind interactions with lunar crustal magnetic anomalies [5], laser-plasma interactions [6], relativistic modeling of a pulsar magnetosphere [7], dusty plasmas [8]–[10], and thruster plasma plumes [11]–[18]. In this method, the charged plasma species are modeled as computational particles, such that each computational particle represents a large number of real ions and electrons. The ion and electron charge densities are computed on a grid at every timestep to solve the Poisson equation and obtain the instantaneous electric potential. Finally, the self-induced electric field is calculated from the gradient of the electric potential and charged particles are moved to new positions using leap-frog integration. But, PIC simulations are computationally expensive, primarily because the simulation timestep is restricted by the electron plasma frequency. For accurate modeling of plasma dynamics, the explicit PIC methods must satisfy the timestep criterion, where $\Delta t < 0.1\omega_{pe}^{-1}$ [4], [19], [20], which is on the order of 0.01 ns for typical ion-thruster conditions with $T_e = 2 \text{ eV}$ and n_e on the order of $10^{15}/\text{m}^3$.

To circumvent the computational expense imposed by fully kinetic electron methods, other works have assumed quasi-neutrality and constant electron temperature which allows the use of a Boltzmann relation for electrons [21]. But, the quasi-neutrality assumption is not valid in the near-field region due to the electrons emitted from an externally mounted neutralizer device which leads to a locally non-neutral plasma. Hybrid fluid-PIC approaches have also been used, such that, the heavy ion species are modeled as particles, and the electrons are modeled as a fluid [12], [22]. But, these electron-fluid models

also require that quasi-neutrality and steady-state be assumed, which may not be applicable for studying the neutralization process in the plasma plume. Other recent studies have allowed for the solution of non-neutral regions in the thruster plume simulation by solving a non-linear Poisson equation and using a polytropic closure for electrons [23]. To minimize the assumptions on the modeling of electron behavior in this article, we use a fully kinetic approach even for electrons.

Simulations with a kinetic approach for electrons were not tractable previously due to the restrictive timestep required for stable plasma simulations. To address the computational expense, we recently developed a multi-GPU PIC-DSMC code called Cuda-based hybrid approach for octree simulation (CHAOS) [24], which exploits the ability of GPUs to improve the computational efficiency of particle-based PIC simulations. Strong scaling studies showed near-ideal scaling for the plume simulations using up to 128 GPUs. Wang *et al.* [25] also performed fully kinetic PIC simulations of a thruster plume with an assumption that the electron–ion sources are colocated. However, in real thruster devices, the externally mounted neutralizer is separated from the xenon ion plume source, and to accurately capture the effect of this configuration on the neutralization mechanism, we performed fully-kinetic plume simulations with separated electron–ion sources and compared the neutralization behavior with the colocated plume [24]. In contrast to the Maxwellian electron kinetics observed for the colocated plume, the electron velocity distribution for the separated electron–ion configuration was non-Maxwellian due to the complex electron trapping mechanism caused by the separation of the sources. However, until now, due to limitations of the traditionally used open boundary conditions (BCs), these neutralization simulations with colocated and separated ion–electron configurations were performed only for early plasma time periods.

The use of fully kinetic electrons in plasma systems that require open boundaries poses a major numerical challenge. Typically, at open boundaries, a homogeneous Neumann BC is applied for the electric field computation, and the particles that cross the boundary are simply removed from the computational domain (also known as an outflow condition). When the beam-front of a fully kinetic thruster plume approaches the exit boundary, the electrons trapped by the positive plume core-region are lost at the beam-front due to the use of this traditional outflow BC for particles. The loss of these trapped electrons causes the self-induced electric field to accelerate the upstream electrons toward the exit boundary. However, these accelerated electrons are also lost due to the outflow particle BC, and this cycle continues until all the electrons are non-physically driven out of the domain. This numerical artifact due to the outflow BC was termed as “numerical pump instability” by Brieda and Wang [26] and Brieda [27]. To avoid these boundary effects, the fully kinetic PIC simulations in our previous work [24] and other fully kinetic works [25], [28], [29] were terminated before the beam-front approached halfway to the exit boundary, prohibiting the study of electron behavior over long temporal scales.

To address the numerical purging of electrons caused by the outflow BC, an ideal solution would be to use infinitely large

domain sizes, especially for thruster plumes that expand into space. But, such domain sizes are computationally intractable. Therefore, an open BC is required that will enable the use of smaller domain sizes to capture electron trapping mechanisms, such that the numerical solution is independent of the domain size with some small tolerance. There has been a considerable effort to determine BCs for plasma sheaths [30]–[32], but not much work is available in the literature on appropriate BCs for use in fully kinetic plasma expansion systems.

Recently, an “ion-sink” open BC was demonstrated using fully kinetic, two-dimensional simulations of ion thruster plasma plumes by Brieda [33], where a virtual sink was implemented midway between the inlet and outlet boundaries. This sink absorbed the ions but allowed the electrons to permeate through it, thus retaining the trapped electrons between the ion sink and the boundary. Electrons were also reflected from the boundary, based on the criterion that the total electrons and ions leaving the domain must be zero. However, the ion sink plane has to be located far from the computational boundary, resulting in an increase in the domain size needed to perform these computations. In addition, the sink was applied to a dimensionally scaled down thruster geometry with domain size on the order of 1 mm, which is smaller than the radius of real-ion thruster devices (on the order of 0.05 m). A current-free BC has also been demonstrated [34] using 2-D simulations of a quasi-neutral plume with colocated ion and electron sources and reduced ion mass ($m_i/m_e = 1826$).

In this article, we propose a new, self-consistent BC for performing fully kinetic simulations of plasma thruster plume expansions that require an open BC, which is sufficiently general, such that it permits the study of thruster plume kinetics at the steady-state using smaller computational domain sizes for both colocated and separated electron–ion configurations. In Section II, we briefly describe the key numerical strategies used in this article that have improved the computational efficiency of fully kinetic plasma plume simulations [24]. We first discuss the non-physical electron removal generated by the widely used outflow BC in Section III-A. Then, in Section III-B, we apply the open BCs available in the literature primarily developed for different plasma applications and objectively show why they fail to conserve the total-charge for the ion-thruster plasma plume application studied in this article. Finally, we describe a newly developed open boundary construct that we call “the charge-conserving energy-based BC” (CCE BC) in Section III-C and compare its performance with the results from other open boundaries implemented using physically motivated criteria for the thruster plume characteristics. To demonstrate its accuracy, we perform simulations of a collisionless mesothermal plume using the CCE BC with colocated ion and electron sources [24] for different domain sizes in Section IV-A. To further demonstrate the generality of the BC and its domain independence, we perform collisionless plume simulations for separated ion and electron sources in Section IV-B, similar to the configuration of real thruster devices. It should be noted that to test and demonstrate the BCs, a two-order of magnitude smaller number density is used for both ion and electrons compared to the real-ion thruster conditions. The higher density calculations have been

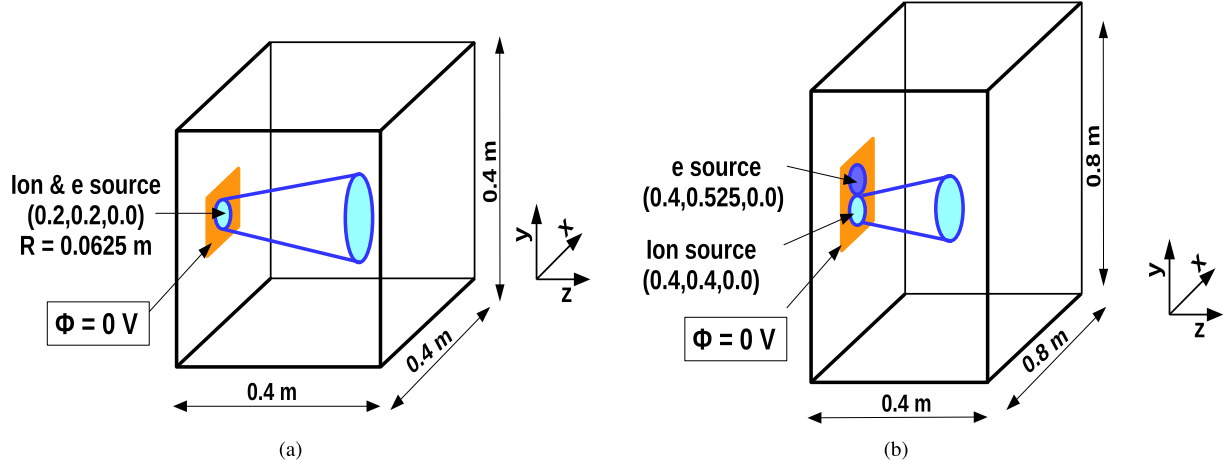


Fig. 1. Simulation setup for the mesothermal plasma plume cases with a domain size of $(0.4 \times 0.4 \times 0.4)$ m for the colocated case and $(0.8 \times 0.8 \times 0.4)$ m for the shifted electron source configuration. A Dirichlet BC of $\phi = 0$ V is implemented in the highlighted orange region in the inlet plane, surrounding the radial sources. (a) Co-located ion-electron source for cases 1 and 2. (b) Electron source shifted above the ion source for case 3.

performed using the proposed open boundary construct to study PIC-DSMC simulations of the ion thruster plume [35].

II. NUMERICAL APPROACH FOR MODELING PIC

CHAOS is an in-house PIC-DSMC solver that we have recently developed to efficiently perform fully kinetic plasma plume simulations [24]. To capture the variation in the local Debye length of the expanding plume, we construct an octree, which is a hierarchical data structure used to store a 3-D AMR grid. In CHAOS, the computational domain is first sub-divided into cells, called roots of the forest of trees (FOTs). Each root is then recursively sub-divided until it satisfies the local Debye length criterion, where the cell size is less than the local Debye length. The final cells that do not undergo further division are called the leaf nodes, while the nodes that underwent division are called internal nodes. To optimize the storage and parallelization efficiency, only the leaf nodes of the FOTs are stored and the internal nodes are discarded [24]. Such a data structure is called a linearized FOT. In addition to the local Debye length criterion, a 2:1 balance condition is imposed, such that all the leaf nodes are, at maximum, only one level coarser than their neighboring leaf nodes [24]. Note that the FOTs are destroyed and re-constructed every 100 timesteps, such that the leaf nodes dynamically satisfy the local Debye length criteria of the evolving plume. Once the flow reaches a steady state, the subsequent PIC steps and macroparameters are computed on the final FOT structure.

At each PIC timestep, the ion and electron particles are mapped to the leaf nodes to compute the total charge density, $\rho = n_i - n_e$, using the nearest grid point method. Note that the linearized Morton-ordered FOTs allows the use of fast bit-wise computations to perform particle-to-grid mapping [24]. Then, the electric potential, ϕ , is computed by using the preconditioned conjugate gradient method to solve the electrostatic Poisson equation. The gradient of the potential is calculated to obtain the induced electric field, which is then applied as an external force to accelerate the charged particles. Finally, the charged particles are moved to new positions based on

the leap-frog scheme which results in a new charge density variation. The above steps are repeated every timestep to track the evolution of the potential and the charged particles. The details of the PIC implementation using multiple CPU-GPU architectures and parallelization, validation studies, and near-ideal strong-scaling performance analysis are discussed in our recent work [24]. This is the first time a fully kinetic 3-D octree-based simulation of ion thruster plumes for real xenon ion-to-electron mass is performed.

In this article, simulations of collisionless, mesothermal, xenon ion plumes are performed with two types of electron source configurations similar to that used in our previous work [24]. In the first configuration, the xenon ion and electron sources are colocated, as shown in Fig. 1(a), and in the second configuration, the electron source is shifted above the ion source, in the y-direction, as shown in Fig. 1(b), to model the externally mounted neutralizer on real thruster devices. It should be noted that a realistic neutralizer also emits neutrals and ions [1], in addition to electrons, but, in this article, we focus only on the effect of electron source location to study the neutralization mechanism, and hence model only the electron emission at the neutralizer source. For these mesothermal simulations, the ratio of initial ion temperature, T_{io} , to the initial electron temperature, T_{eo} , is 0.01. Electrons are initialized at the source with a stationary half-Maxwellian distribution in the streamwise and full-Maxwellian in the cross-stream directions with $T_{eo} = 2$ eV and an initial number density of $n_{eo} = 1.0 \times 10^{13}/\text{m}^3$, similar to previous mesothermal studies [24], [25]. These selected values for T_{eo} and n_{eo} result in an initial Debye length, $\lambda_{do} = 3.32 \times 10^{-3}$ m, initial electron plasma frequency, $\omega_{peo} = 1.78 \times 10^8$ rad/s, and initial electron thermal velocity, $v_{teo} = 592,892$ m/s. The ratio of initial ion to electron number densities, $n_{io}/n_{eo} = 4$, is similar to that used in previous work [24] for the colocated case ensuring a current-free condition at the inlet [25]. However, as the plume evolves, it is neutralized such that the electron and ion densities become equal. For the case with a shifted electron source, the ratio of n_{io}/n_{eo} is initially equal to unity

by ensuring that the charge density at the respective sources is equal. The ions are initialized with a drifting Maxwellian distribution with a beam velocity of 30 000 m/s, which is typical for ion thruster plumes. The input parameters used for the simulations are given in Tables III and IV in Appendix A.

The radius, R , of the ion and electron sources in both the configurations, shown in Fig. 1, is equal to 0.0625 m, representative of real thruster devices [1]. The size of the 3-D domain is chosen to be equal to $(0.4 \times 0.4 \times 0.4)$ m for the colocated case, and $(0.8 \times 0.8 \times 0.4)$ m for the separated electron-ion configuration case. Note that the center of the ion source is located at the center of the inlet plane for both the cases and the electron source center is shifted above the ion source by one diameter length in the second configuration. A Dirichlet BC with $\phi = 0$ V is applied in the region surrounding the sources to model the thruster surface surrounding the ion and electron sources, as shown by the highlighted orange region in Fig. 1 and a homogeneous Neumann BC is applied everywhere else along the inlet plane of the electric field. The homogeneous BC at the source is consistent with the current-free initial conditions for the colocated case, and for the separated ion-electron case, we assume that the potential gradient normal to the inlet boundary is negligible. The particle and electric-field BCs at all the other open boundaries (cross-stream boundaries and $z = z_{\max}$ boundary) required to perform stable, steady-state plume simulations are discussed and analyzed in Section III.

III. ANALYSIS OF OPEN BCs

The criterion to assess the success of an open BC for this article, is that when the plume beam-front crosses the computational domain, the plume should continue to be stable, steady, and for the colocated case, resulting in a quasi-neutral plume, as observed from previous work [24], [25], where the simulations were terminated before the plume reached a steady-state to prevent boundary effects. Additionally, the BC should also be sufficiently general to perform simulations with a shifted electron source, similar to real thrusters with an externally mounted neutralizer, where the quasi-neutrality assumption is not valid [24], particularly in the near-field.

A. Outflow BC

In the traditional open BC used to model the plasma plume expansion into the vacuum of space, particles that cross the computational domain are removed from the simulation, called outflow B.C., and a homogeneous Neumann electric field BC is implemented. The transient evolution of the ion and electron charge density distributions using the outflow boundary at $t\omega_{\text{peo}} = 600, 1000, 1500$, and 2500 are shown in Fig. 2(a)–(d), respectively. Since the colocated plume is symmetric, the ion and electron charge densities are shown above and below the plume centerline, respectively, in Fig. 2(a)–(d). Initially, at $t\omega_{\text{peo}} = 600$ and 1000 , the electrons travel faster and overshoot the ion beam in the streamwise direction. At $t\omega_{\text{peo}} = 1500$, the electrons become trapped within the plume, such that the leading edge of the ion and electron charge densities is aligned. However, there is still

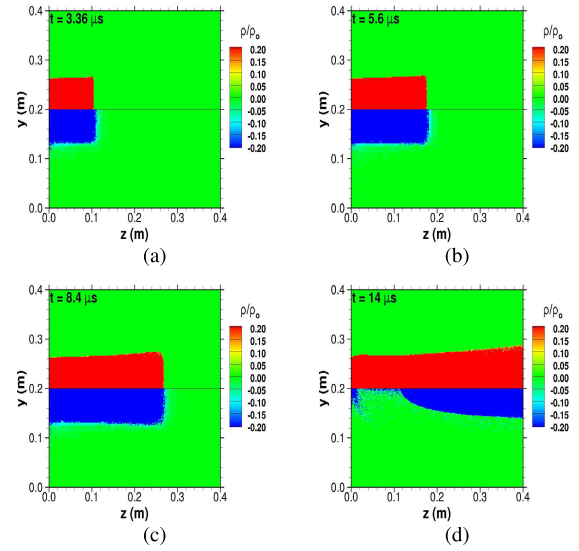


Fig. 2. Transient ion and electron charge density variations along the YZ plane extracted at the center of the domain obtained using outflow open BC, normalized by $\rho_0 = e \cdot n_e$. (a) $t\omega_{\text{peo}} = 600$. (b) $t\omega_{\text{peo}} = 1000$. (c) $t\omega_{\text{peo}} = 1500$. (d) $t\omega_{\text{peo}} = 2500$.

a small fraction of electrons downstream of the ion beam-front. As the ion beam-front approaches the boundary, these leading electrons are lost. To compensate for the local charge imbalance caused by the loss of the trapped electrons, the self-consistent electric field accelerates the upstream electrons toward the boundary in a non-physical manner. However, eventually, these electrons are also lost due to the outflow particle BC, which further increases the electron acceleration, until all the electrons are removed from the domain, as shown by the decrease in the electron charge density close to the colocated source, shown in Fig. 2(d).

The non-physical effect of the outflow BC on the electron kinetic behavior is analyzed by sampling the electron velocity distribution functions (EVDFs) at $z = 0.2$ m, which is midway between the inlet and outlet domain boundaries and at the beam-front location, within 0.05-m radius from the plume-axis that is along the line defined by co-ordinates $(0.2, 0.2, z)$. Note that at $t\omega_{\text{peo}} = 2000$ and 2200 , the beam-front is located at $z = 0.34$ and 0.4 m, respectively, and at $t\omega_{\text{peo}} = 2400$, since the beam-front has crossed the computational boundary, the EVDF is sampled at $z = 0.4$ m. The evolution of the sampled z -EVDF at the beam-front and at $z = 0.2$ m, as the beam-front approaches the computational boundary, is shown in Fig. 3(a) and (b), respectively. When the beam-front is at $z = 0.34$ m, at $t\omega_{\text{peo}} = 2000$, the sampled z -EVDF agrees well with the analytical Maxwellian distribution for $T_e = 1.5$ eV and a bulk velocity of 30 000 m/s, which is equal to the ion beam velocity. This agreement of the z -EVDF with the analytical Maxwellian shows that the electrons at the beam-front are electrostatically trapped by the ion beam and are collectively traveling with the ion beam velocity. However, at $t\omega_{\text{peo}} = 2200$, as the beam-front approaches the domain boundary at $z = 0.4$ m, we observe that the sampled EVDF is no longer Maxwellian. In particular, very few electrons

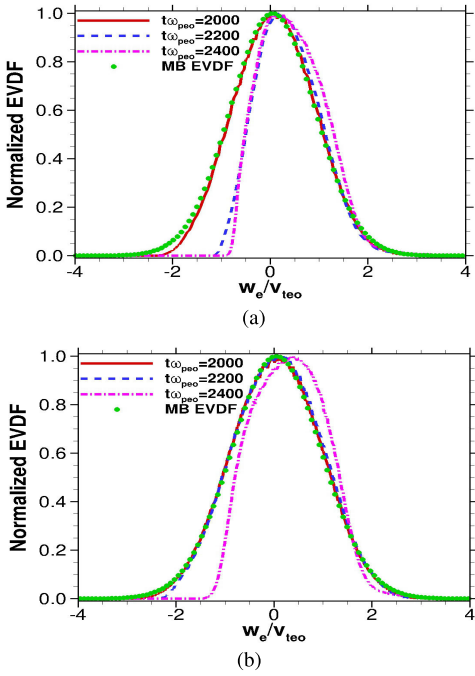


Fig. 3. Evolution of the z -EVDF normalized by v_{teo} at the beam-front and $z = 0.2$ m as the beam-front approaches the z_{\max} domain boundary compared with the analytical Maxwell Boltzmann (MB) distribution at $T_e = 1.5$ eV. (a) z -EVDF at the beam-front. (b) z -EVDF at $z = 0.2$ m.

have negative velocity, as observed from the z -EVDF, which indicates that most of the electrons are accelerated toward the exit boundary to balance the loss of the trapped electrons. Since these accelerated electrons are also lost at the boundary, the z -EVDF at $t_{\omega_{peo}} = 2400$ shifts to the right, indicating further acceleration of electrons out of the domain.

The effect of this sustained loss of trapped electrons at the boundary is also found to influence the z -EVDF up-stream of the boundary. From Fig. 3(b), we observe that between $t_{\omega_{peo}} = 2000$ and 2200, the z -EVDF of the electrons sampled at $z = 0.2$ m agrees well with the analytical Maxwellian distribution at $T_e = 1.7$ eV and at a bulk velocity of 30 000 m/s. It can be inferred that at $t_{\omega_{peo}} = 2000$, the z -component of the electron temperature decreases from $T_{ez} = 1.7$ eV at $z = 0.2$ m to $T_{ez} = 1.5$ eV at $z = 0.34$ due to plume expansion. At $t_{\omega_{peo}} = 2200$, even though the z -EVDF at $z = 0.4$ m indicates acceleration, the upstream z -EVDF at $z = 0.2$ m agrees well with the Maxwellian. However, at $t_{\omega_{peo}} = 2400$, the upstream electrons at $z = 0.2$ m also undergo acceleration in the streamwise direction, as indicated by the shift in the z -EVDF, with the peak value at $w_e/v_{teo} = 0.5$, which is equal to a bulk velocity of 296 446 m/s. A high bulk velocity indicates an accelerated removal of electrons until finally the electron charge density becomes zero in the domain.

B. Buffer BC

To prevent the non-physical removal of the trapped electrons, we first implement an open boundary construct, called the “buffer BC,” proposed by Klimas *et al.* [36], who used this BC for PIC simulations of collisionless magnetic reconnection processes. Fig. 4 shows a schematic of the approach applied to

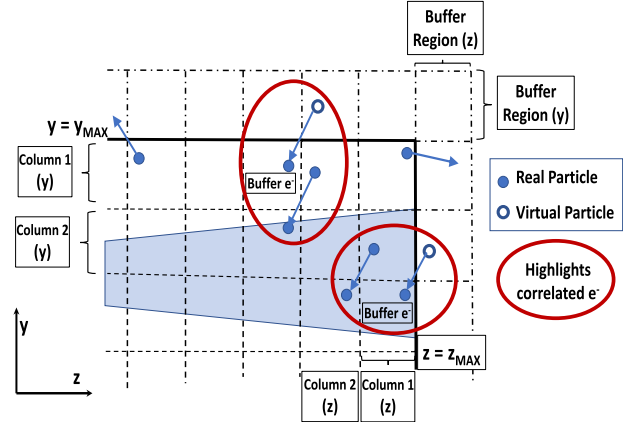


Fig. 4. Illustration of the buffer BC.

the electrostatic expansion of the thruster plume studied in this article. As an extension of their method [36] to an octree grid, a layer of octree leaf nodes adjacent to the domain boundaries ($x_{\min}, y_{\min}, x_{\max}, y_{\max}, z_{\min}, z_{\max}$) is termed column 1 and a layer of leaf nodes immediately upstream of column 1 is termed column 2. The region adjacent to the boundary, outside of the domain, which is not modeled in the simulation is called the “ghost” or “buffer” region, as shown for the y_{\max} and z_{\max} boundary in the schematic. In the buffer BC approach, it is assumed that if an electron moves from column 1 to 2, then there would be an identical twin electron particle that would move from the “ghost” or “buffer” region into the leaf nodes that belong to column 1. This BC results in an influx of electrons, which are called “buffer” electrons at the boundary with a velocity equal to the electron that has moved from column 1 to 2 and with a relative position similar to that in column 2, shifted by one cell length, such that its position is in column 1. The re-entering “buffer” electron particles are clones of those particles that moved from column 1 to 2, which are highlighted by a red circle in Fig. 4. Note that the trapped electrons exhibit a distribution with both positive and negative velocities, as observed earlier in Fig. 3, and therefore we expect electrons to have negative w_e velocities at the z_{\max} boundary that will generate “buffer” electrons. A similar treatment for the electrons is also implemented at the other open cross-stream boundaries, ($x_{\min}, y_{\min}, x_{\max}, y_{\max}$). At the inlet plane boundary, i.e., the $z = 0$ plane, the traditional outflow boundary is implemented for all the particles, wherein the particles that cross the boundary with negative z -velocities are deleted from the simulation. To compute the electric field, a Dirichlet BC of $\phi = 0$ V is implemented in the region surrounding the thruster exit, and everywhere else along the inlet plane, a homogeneous Neumann BC is implemented, as shown earlier in Fig. 1(a).

Unlike the work of Klimas *et al.* [36], the “buffer” electrons are not allowed to reenter from the z_{\max} boundary for every timestep in this article. If the buffer BC was invoked every timestep at the $z = z_{\max}$ boundary, the buffer electrons that were introduced in the previous timestep would move from column 1 to 2 in the subsequent timestep due to their negative velocities, which would result in new “buffer” electrons

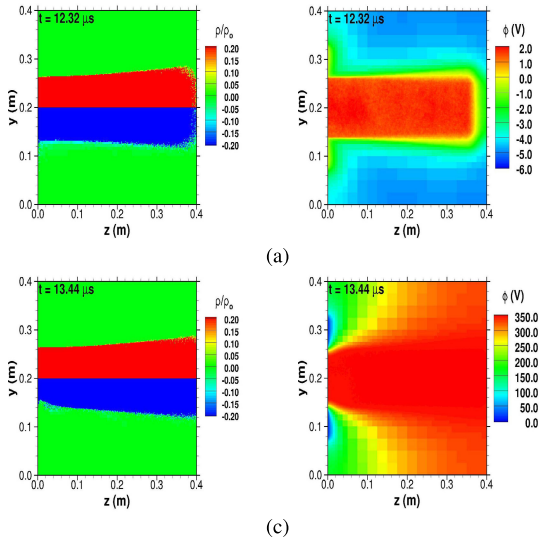


Fig. 5. Transient evolution of ion (top) and electron (bottom) charge density variations and electric potential variation obtained from the buffer BC simulation along the YZ plane extracted at the center of the domain. (a) Ion and electron charge densities normalized by $\rho_o = e.n_{eo}$ at $t\omega_{peo} = 2200$. (b) Instantaneous electric potential variation at $t\omega_{peo} = 2200$. (c) Ion and electron charge densities normalized by $\rho_o = e.n_{eo}$ at $t\omega_{peo} = 2400$. Instantaneous electric potential variation at $t\omega_{peo} = 2400$.

entering the computational domain, with the same velocity and relative position. Such repetitive cloning of electrons would lead to a strong correlation between the electrons, and it would eventually bias the z -EVDF to have a negative bulk velocity, instead of maintaining the bulk z -EVDF equal to the ion beam velocity, as was observed for the electrons that were trapped within the plume. Note that in the work of Klimas *et al.* [36], a strong correlation did not disturb the solution within the interior region of the domain for magnetic reconnection studies. In this article, to avoid a negative bulk velocity of electrons due to strong correlations, the buffer BC is invoked at alternate timesteps at the z_{\max} boundary, allowing sufficient time for the newly entered electrons to cross column 1. However, at the cross-stream boundaries, the buffer BC is performed at every timestep since the electron flux leaving these boundaries is small compared to the $z = z_{\max}$ boundary. At the cross-stream boundaries and z_{\max} boundaries, as shown in Fig. 4, the inhomogeneous Neumann BC,

$$\left(\frac{\partial \phi}{\partial n}\right)_b^k = \frac{q(N_{i,b} - N_{e,b})^k}{A_b \epsilon_0} \quad (1)$$

is implemented at every boundary cell, b , where $(\partial \phi / \partial n)^k$ is the normal potential gradient at the boundary cell b at the k th timestep; q and ϵ_0 are the electric charge and permittivity of free space; respectively, $N_{i,b}$ and $N_{e,b}$ are the number of ions and electrons that cross the boundary cell b at the k th timestep; and A_b is the area of the z_{\max} face of the b th boundary cell.

The transient evolution of the symmetric plume from the time when the beam-front crosses the boundary, i.e., $t\omega_{peo} = 2200$ to the instant when it becomes unstable, i.e., $t\omega_{peo} = 2400$, using the buffer BC is shown in Fig. 5. The instantaneous ion and electron charge density variations

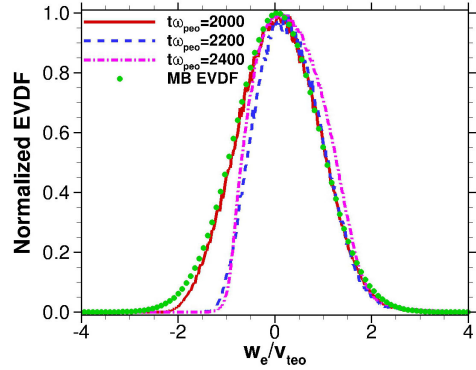


Fig. 6. Evolution of the z -EVDF at the beam-front, normalized by v_{teo} , as it crosses the z_{\max} domain boundary using the buffer BC.

at $t\omega_{peo} = 2200$ along the yz plane, extracted at the center of the domain, is shown in Fig. 5(a). It can be seen that the ion beam-front has reached the domain boundary, and the ion and electron charge distributions are equivalent. The plume is quasi-neutral as seen from the corresponding instantaneous electric potential at $t\omega_{peo} = 2200$, shown in Fig. 5(b). However, as the plume continues to evolve, at $t\omega_{peo} = 2400$, the electron charge distribution near the colocated source decreases compared to the ion charge density, as shown in Fig. 5(c), due to the loss of trapped electrons at the open boundary. As a result of this decrease in the electron charge density, the instantaneous electric potential blows up to a non-physical value of 350 V within just 200 plasma time periods.

The reason for the failure of the “buffer BC” to retain the trapped electrons can be better understood by sampling the EVDF at the beam-front, as the plume approaches the boundary, similar to the analysis discussed in Section III-A. Fig. 6 shows the z -EVDF at the beam-front as it progresses from $z = 0.34$ at $t\omega_{peo} = 2000$ to crossing the boundary at $t\omega_{peo} = 2400$. Similar to the outflow B.C., the z -EVDF at the boundary is not Maxwellian at $t\omega_{peo} = 2200$ and 2400, and indicates that most of the trapped electrons in the beam-front leave the domain due to the positive streamwise velocity. Thus, an insufficient number of electrons have negative velocity, which in turn causes fewer electrons to move from column 1 to column 2. Furthermore, the bias in the EVDF indicates that there will be a rapid loss of trapped electrons at the boundary similar to the outflow BC, which in turn will further accelerate electrons in the positive z -direction increasing the bias in the z -EVDF. Since the buffer BC at the z_{\max} boundary is imposed at alternate timesteps to avoid strong correlation, the charge-imbalance at the boundary increases rapidly, and all the electrons are driven out of the domain.

The buffer BC failed to trap electrons because of its inability to explicitly correct for the local charge imbalance and maintain the total charge in the domain, leading to an accelerated non-physical purging of electrons out of the computational domain. In addition to the buffer BC, we also performed simulations with pure reflection and influx BCs to demonstrate why a new open-boundary construct was required. Table I summarizes the different treatments for electron particles implemented at the domain boundaries considered in this

article, namely the buffer, reflection, influx, and CCE BCs. For all the BCs presented, a non-homogeneous BC defined in (1) is implemented at the cross-stream and $z = z_{\max}$ boundaries. In addition, the buffer electrons are implemented at the cross-stream boundaries for all the BCs. The pure reflection BC was employed to enforce the electron trapping at the z_{\max} boundary and prevent the loss of trapped electrons at the z_{\max} boundary, as a means of increasing the number of electrons in the negative tail-end of the z -EVDF shown in Fig. 6. In this strategy, electrons crossing the z_{\max} boundary with energy less than the initial energy of 2 eV were reflected. Although this BC prevented the loss of electrons, it did not satisfy the quasi-neutrality criterion that is expected for a colocated plume, because it decreased the total charge in the domain since the criterion used to reflect electrons assumed an electron energy distribution of 2 eV at the z_{\max} boundary. However, due to expansion, the average energy of electrons at the downstream z_{\max} boundary is lower than the initial value at the source, which leads to a higher number of electrons in the domain.

An influx BC was also used to analyze the potential benefits of implementing charge conservation without an energy-conservation treatment for electrons. For this BC, the total baseline charge in the domain was computed before the beam-front crossed the domain, and this baseline charge was maintained by introducing additional electrons at the inlet such that the total charge was conserved. Although the macroparameters, such as the potential and charge densities, were stable due to the conservation of the total charge in the domain, the influx open boundary construct did not maintain a physically reasonable EVDF. The additional electrons that were introduced at the inlet altered the electron velocity distribution to have a very high bulk velocity of 1 eV, which is much higher than the expected EVDF with bulk velocity equal to the ion bulk velocity of 0.05 eV. The details of the reflection and influx BC and the reason for their failure are discussed further in Appendix B. The details of the newly developed CCE BC that is capable of conserving the total charge and predict physically accurate EVDFs are discussed in Section III-C.

C. Total CCE BC

Generation of a stable steady-state plume without altering the electron kinetics requires an energy-based treatment for the electrons at the boundary in addition to conservation of the total charge in the domain. In the CCE BC, when the beam-front crosses the region located $4\lambda_D$ upstream of the domain boundary, the baseline total charge, Q , and the average electron energy, $\langle E_{el} \rangle$, are computed as

$$Q = q(N_i - N_e) \quad (2)$$

$$\langle E_{el} \rangle = \frac{1}{N_e} \sum_{j=0}^{j < N_e} \frac{1}{2}(u_j^2 + v_j^2 + w_j^2) \quad (3)$$

where q is the elementary charge, N_e and N_i are, respectively, the total number of electrons and ions in the domain, and u_j , v_j , and w_j are the x -, y -, and z -velocity components of the j th electron, respectively. At all subsequent timesteps,

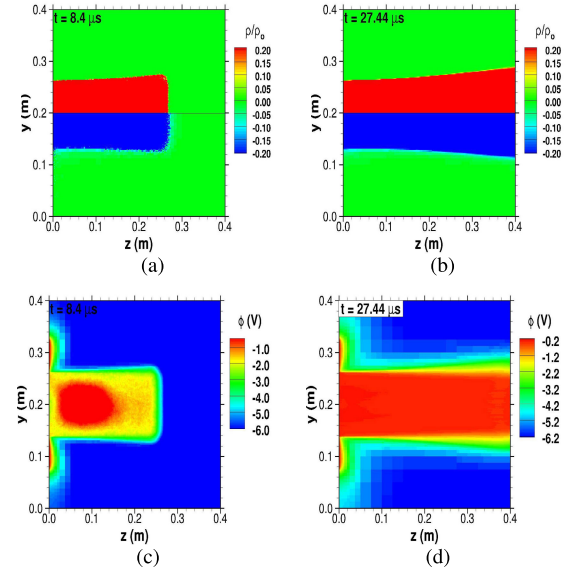


Fig. 7. Transient ion and electron charge density variations normalized by ρ_0 and the corresponding electric potential obtained using the CCE BC. (a) Normalized charge density at $t\omega_{peo} = 1500$. (b) Normalized charge density at $t\omega_{peo} = 4900$. (c) Electric potential at $t\omega_{peo} = 1500$. (d) Sampled electric potential $t\omega_{peo} = 4900$.

the baseline charge, Q , is maintained by monitoring the instantaneous total charge, Q^k , at the k th timestep. If $Q^k > Q$, then electrons are specularly reflected from the z_{\max} boundary, instead of introducing them from the electron source which alters the flux and the EVDF of the electrons as previously discussed. But, unlike the reflection BC, where, electrons were reflected based on a thermal energy equivalent to $T_e = 2$ eV, in this case, only those electrons with kinetic energy less than the baseline average energy $\langle E_{el} \rangle$ are specularly reflected.

It should be noted that the criterion for electron reflection in the CCE BC does not assume a Maxwellian distribution for electrons, since the baseline energy is not obtained from the temperature, and therefore can be used even for thruster plume simulations with a separated electron-ion configuration. If $Q^k < Q$, then the electrons that leave the $z = z_{\max}$ boundary are deleted, similar to the outflow BC. At the cross-stream boundaries, the buffer particle BC is implemented, such that, if electrons move toward the interior of the domain from the layer of cells adjacent to the boundary, then new electrons are introduced at the cross-stream domain boundary cells, as described in the footnote of Table I. The electric field BC is the same as that discussed earlier in Section III-B and Table I.

To analyze the stability of the plume modeled using the CCE BC as it evolves to a steady state, the transient snapshots of the ion and electron charge density distributions at $t\omega_{peo} = 1500$ and 4900 are shown in Fig. 7(a) and (b), respectively. The densities are extracted along the yz plane passing through the center of the domain, and since the colocated plume is symmetric, the ion and electron density variations are shown above and below the plume center-line, respectively. It can be observed that at $t\omega_{peo} = 1500$, both the ion and electron species show similar spatial variation, and this equivalence in the density variation of the charged species is

TABLE I
DESCRIPTION OF THE ELECTRON PARTICLE TREATMENTS AT THE DOMAIN BOUNDARIES IMPLEMENTED FOR DIFFERENT BCs^a

BC	At $z = z_{max}$	Additional particle introduction at $z = z_{min}$
Buffer	Buffer electrons at alternate timesteps	-
Reflection	If number of outgoing electrons > outgoing ions, electrons with $K.E. < (3/2)k_b T_{eo}$ are reflected. No Buffer at $z = z_{max}$.	-
Influx ^b	Only outflow. No Buffer at $z = z_{max}$. No electron reflection.	If $Q^k > Q$, additional electrons introduced from source.
CCE ^b	If $Q^k > Q$, then electrons with $K.E. < \langle E_{el} \rangle$ are specularly reflected ^c .	-

^aFor all BCs, buffer electrons are implemented for all BCs at cross-stream boundaries, $x_{min}, x_{max}, y_{min}, y_{max}$, non-homogeneous electric field BC, given in Eq. (1), is implemented at the cross-stream and $z = z_{max}$ boundaries, at the $z = 0$ inlet place, Dirichlet BC $\phi=0$ V is implemented at the orange region, shown in Fig. 1, and, particles crossing $z = 0$ inlet plane are deleted from the computational domain.

^bBaseline total charge, Q , computed when beam-front is $4\lambda_D$ upstream of $z = z_{max}$ and Q^k at timestep k is monitored

^c $K.E.$ is kinetic energy of an individual electron particle, $\langle E_{el} \rangle$ is average electron kinetic energy in the domain. (Eq. (3))

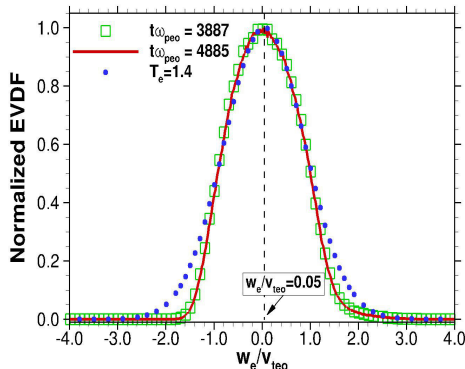


Fig. 8. z -EVDF of electrons at $z = 0.1$ m obtained using the CCE BC at the steady state.

maintained even at $t\omega_{peo} = 4900$, which is 3400 plasma time periods after the beam-front initially crosses the boundary. The charge-conserving, energy-based, open BC, implemented in the $z = z_{max}$ plane has maintained the electron number density and has prevented the loss of electrons that was observed in the outflow and buffer BC, shown previously in Figs. 2(d) and 5(c), respectively. The corresponding electric potential at $t\omega_{peo} = 1500$ and 4900 is shown in Fig. 7(c) and (d), respectively. At $t\omega_{peo} = 1500$, the electrostatic coupling between the ions and electrons entraps the electrons, and eventually, at $t\omega_{peo} = 4900$, the sampled steady-state potential is quasi-neutral within the plume. Note that the electric potential surrounding the colocated source in the inlet plane is close to 0 V, due to the Dirichlet BC used to model the thruster surface, as shown previously by the shaded orange region in Fig. 1(a).

To determine if the plume has reached a steady-state, we compare the instantaneous z -EVDF at $z = 0.1$ m, obtained at 21.84 and 27.44 μ s, corresponding to plasma time periods of $t\omega_{peo} = 3.800$ and 4800, respectively. As shown in Fig. 8, the agreement of the z -EVDFs at $z = 0.1$ m sampled at $t\omega_{peo} = 3.800$ and 4800 indicates that the flow has reached

a steady state. Comparing the sampled EVDF with the analytically computed Maxwellian, it is observed that the z -EVDF at $z = 0.1$ m has a thermal component of 1.2 eV and since the peak is located at $w_e/v_{teo} = 0.05$, the electrons collectively travel with the ion beam-velocity of 30 000 m/s at the steady state. The EVDF obtained from simulation is a bit narrower than the analytical EVDF for $|w_e/v_{teo}| > 1.5$, because only those electrons with energy less than the average energy were reflected at the $z = z_{max}$ boundary. As a consequence, there are fewer energetic electrons at the tail of the distribution. Note that using the average electron energy as the criterion for electron reflection is physically reasonable, since the electrons with higher energy will not remain electrostatically trapped within the core of the plume, as was also observed by the comparatively narrow tail distribution of the beam-front EVDF sampled at $z = 0.34$ m for $t\omega_{peo} = 2000$, shown earlier in Fig. 6.

Table II summarizes the performance of the above-discussed open BCs in terms of satisfying the main criteria used to assess the accuracy of the open BC, based on the known characteristics of the colocated plume. It can be seen that the CCE BC satisfied all four criteria. Specifically, it results in a stable, steady plume with quasi-neutral potential as well as Maxwellian EVDF for the colocated case. The CCE BC is general, as it does not assume neutrality or a Maxwellian distribution for the electrons.

IV. DOMAIN-INDEPENDENCE STUDIES WITH CCE BC

Collisionless thruster plume simulations are performed to demonstrate convergence and domain independence of the electric potential and EVDF in the near-field, using the CCE BC for the colocated as well as separated electron and ion source configurations shown in Fig. 1. The domain-independence studies for the colocated case are performed using domain sizes of $(0.4 \times 0.4 \times 0.4)$ m and $(0.8 \times 0.8 \times 0.8)$ m, while for the separated electron-ion configuration, simulations are performed for domain sizes of $(0.8 \times 0.8 \times 0.4)$, $(0.8 \times 0.8 \times 0.8)$, and $(1.0 \times 1.0 \times 1.0)$ m.

TABLE II
SUMMARY OF THE PERFORMANCE OF THE BCs IN TERMS OF THE CRITERIA USED TO ASSESS THEIR ACCURACY

Criteria	Stable Plume	Neutrality? (colocated)	Maxwellian EVDF? (colocated)	Steady-state?
Buffer	✗			
Reflection	✓	✗		
Influx	✓	✓	✗	
CCE	✓	✓	✓	✓

A. Colocated Case

Macroparameters for the 0.4- and 0.8-m domain cases with colocated ion-electron sources are sampled for 80000 timesteps after the flow has reached a steady-state. As is shown in Fig. 8, the electric potential and EVDF reach a steady state at $t\omega_{peo} = 3.900$, well before starting the macroparameter sampling at $t\omega_{peo} = 5000$. The variation of the total number of ions and electrons in the domain with an increase in the timestep is shown for all the colocated plume simulations in Fig. 18 in Appendix C. A comparison of the steady-state electric potential variation extracted along the yz plane passing through the center of the $(0.4 \times 0.4 \times 0.4)$ and $(0.8 \times 0.8 \times 0.8)$ m domains is shown in Fig. 9(a). It can be seen that the shape of the symmetric colocated plume obtained from both the 0.4- and 0.8-m domain simulations are in agreement. For a more quantifiable comparison, the steady-state charge density and electric potential are extracted along a line passing through the center of the plume, i.e., along the axis of symmetry. The variation of the ion and electron charge densities, normalized by the initial electron charge density, $\rho_o = e \cdot n_{eo}$, as well as the electric potential along this plume center-line is shown in Fig. 9(b). The comparison along the plume center-line obtained from the 0.4- and 0.8-m domains shows that the electron and ion charge densities are equal in magnitude and opposite in charge, indicating that the plume is quasi-neutral. Also, the charge density variation along the center-line obtained from the 0.4-m case agrees within 2% with that from the 0.8-m simulation, suggesting that the number densities in the domain are converged and independent of the domain size.

It should be noted that the plume center-line electric potential from the 0.4-m domain simulation is 0.38 V lower compared to the 0.8-m domain simulation. This small difference in the electric potential may have been caused by the noise due to the number of particles escaping from the cross-stream boundary. At the cross-stream boundary, even though the number density of the charged particles is in agreement, as shown in Fig. 10(a), the number of particles per cell at the boundary is 50 and 250 for the 0.4- and 0.8-m simulations, respectively, due to over-refinement of leaf nodes for the 0.4-m domain. These variations in the value of outgoing number of electrons affect the computation of the local Neumann BC at the boundary cells (1), which in turn affects the global Poisson's solution for electric potential throughout the simulation domain. Nevertheless, it can be seen that the potential gradient obtained from the two simulations is in agreement and the comparisons demonstrate that the CCE BC provides

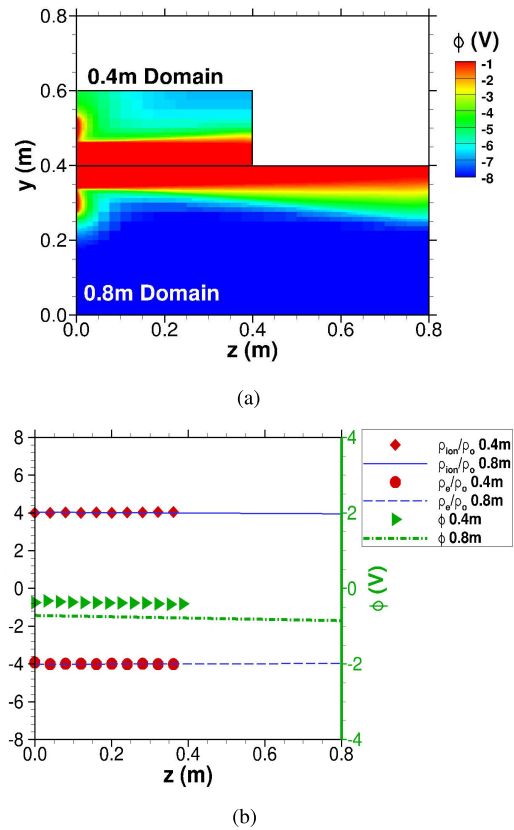


Fig. 9. Comparison of electric potential and normalized ion and electron charge densities obtained from the 0.4- and 0.8-m domains for the co-located ion-electron source case. (a) Potential variation along the yz plane at the center of the domain. (b) Charge density variation and electric potential along the plume center line.

a domain-independent solution within a tolerance of 2.4 V at the boundary and 0.4 V at the core of the plume. It should also be noted that for PIC simulations, the fluctuations in Poisson's solution, i.e., ϕ , varies as $(\sqrt{N_e})^{-1}$, where N_e is the number of electrons per cell [37] and the small difference in the electric potential observed for the 0.4- and 0.8-m simulations is within the acceptable tolerance for particle-based methods.

To compare the width of the plume expansion and the variation of charge density near the cross-stream boundaries, the flow-field macroparameters are extracted along a line at $z = 0.4$ m on the yz plane. The comparison of the normalized ion and electron charge densities obtained from the 0.4- and 0.8-m simulations is shown in Fig. 10(a) and are in good agreement, suggesting that the plume expansion width from the two simulations is equal. It can also be observed that

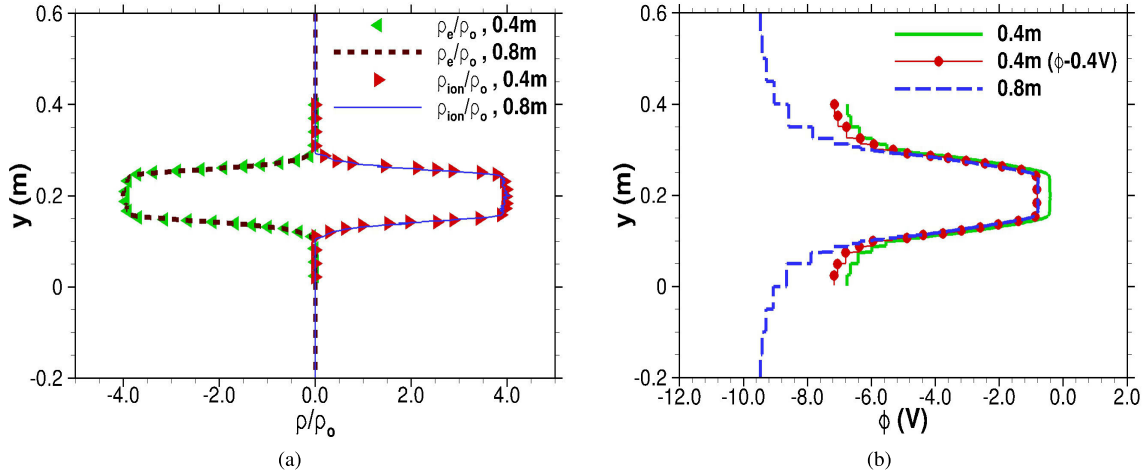


Fig. 10. Comparison of ion and electron charge densities and electric potential along a vertical line extracted at $z = 0.4$ m in the yz plane obtained from the colocated cases with 0.4- and 0.8-m domains. (a) Ion and electron charge density variations normalized by ρ_0 . (b) Electric potential variation.

the normalized ion and electron charge densities within the plume are equal in magnitude and opposite in charge as well as symmetric about the center, $y = 0.2$, since the plume for the colocated ion and electric sources is symmetric.

A comparison of potential variation along the $z = 0.4$ m line obtained from the 0.4- and 0.8-m simulations is shown in Fig. 10(b). As mentioned previously, the potential obtained from the 0.4-m case is lower by 0.4 V; therefore, to compare the shape of the potential variation along the radial direction, the potential from the 0.4-m simulation is shifted by -0.4 V. The trend in the potential variation from the small and large domain cases agrees well in the core region of the plume, which extends from $y = 0.1$ m to $y = 0.3$ m. However, at the cross-stream y -boundaries, the potential from the 0.4-m domain simulation is 2 V higher (less negative) compared to that of the 0.8-m domain simulation. This difference in the boundary potential is again due to the statistical fluctuations in the number of electrons that escapes from the boundary that affects the Neumann BC and the corresponding Poisson's solution.

To study the effect of domain size on electron kinetics, EVDFs are sampled at $z = 0.01$ and 0.2 m, i.e., near the source and midway between the source and the boundary, within a 0.05-m radius from the plume center-line. A comparison of the y -EVDF, at $z = 0.01$ m, from the 0.4- and 0.8-m simulations is shown in Fig. 11(a), along with the analytical Maxwellian distributions generated to match with the sampled EVDFs. The y -EVDF from the 0.4-m simulation is 0.15 eV cooler than that of the 0.8-m simulation, which agrees with a Maxwellian distribution of $T_{ey} = 1.35$ eV. The temperature in the cross-stream direction is less than the initial temperature of 2 eV, because the plume expands in the radial direction. Since the colocated plume is symmetric, the x - and y -EVDFs are found to be equal.

Unlike the y -EVDF, the z -EVDF at $z = 0.01$ m is not strictly Maxwellian as shown in Fig. 11(b). Because the electrons are introduced at the source with an initial thermal velocity which is an order of magnitude higher than the ion

beam velocity, the plume at the source initially has a higher positive charge. However, this positive charge electrostatically traps electrons by slowing them and reversing their direction, as indicated by the secondary peak at $w_e/v_{teo} = -0.05$. This double peak behavior of electrons at the source is observed for both the 0.4- and 0.8-m simulations, suggesting that the electron trapping is independent of the domain size. However, similar to the y -EVDF comparison, the thermal energy of the z -EVDF from the 0.4-m simulation is approximately 0.15 eV less than that of the 0.8-m simulation. This difference in the energy is caused by the lower potential gradient in the y -direction obtained from the 0.4-m case compared to the 0.8-m case shown in Fig. 10(b), which, in turn, results in lower acceleration compared to the 0.8-m simulation. It should also be noted that the electron temperature is anisotropic, since the y - and z -EVDFs are not equal, which is contrary to the constant and isotropic electron temperature used in the Boltzmann approximation.

Downstream from the source region, at $z = 0.2$ m, the z -EVDF obtained from the 0.4- and 0.8-m simulations are found to be Maxwellian, as shown in Fig. 11(c), unlike the double peak distribution at $z = 0.01$ m shown in Fig. 11(b). The z -EVDF from the 0.4-m simulation agrees well with a Maxwellian distribution of $T_{ez} = 1.4$ eV and a bulk velocity of $w_e/v_{teo} = 0.05$, which is equal to the ion beam velocity of 30000 m/s. This agreement indicates that the electrons that are emitted with an initial stationary half-Maxwellian in z and full-Maxwellian in x - and y -directions are trapped within the plume, such that the electrons collectively propagate with the ion beam. A similar trapping mechanism with the bulk electron velocity equal to the ion beam velocity is also observed from the 0.8-m simulation. However, the T_{ez} of the 0.4-m simulation is 0.1 eV less than that of the 0.8-m case, as shown in Fig. 11(c). The retention of low energy electrons from the 0.4-m simulation suggests that the average energy of the smaller domain case, used as a criterion to reflect electrons, is less than that used in the 0.8-m simulation. As a result, the number of electrons reflected at the $z = z_{max}$ boundary is

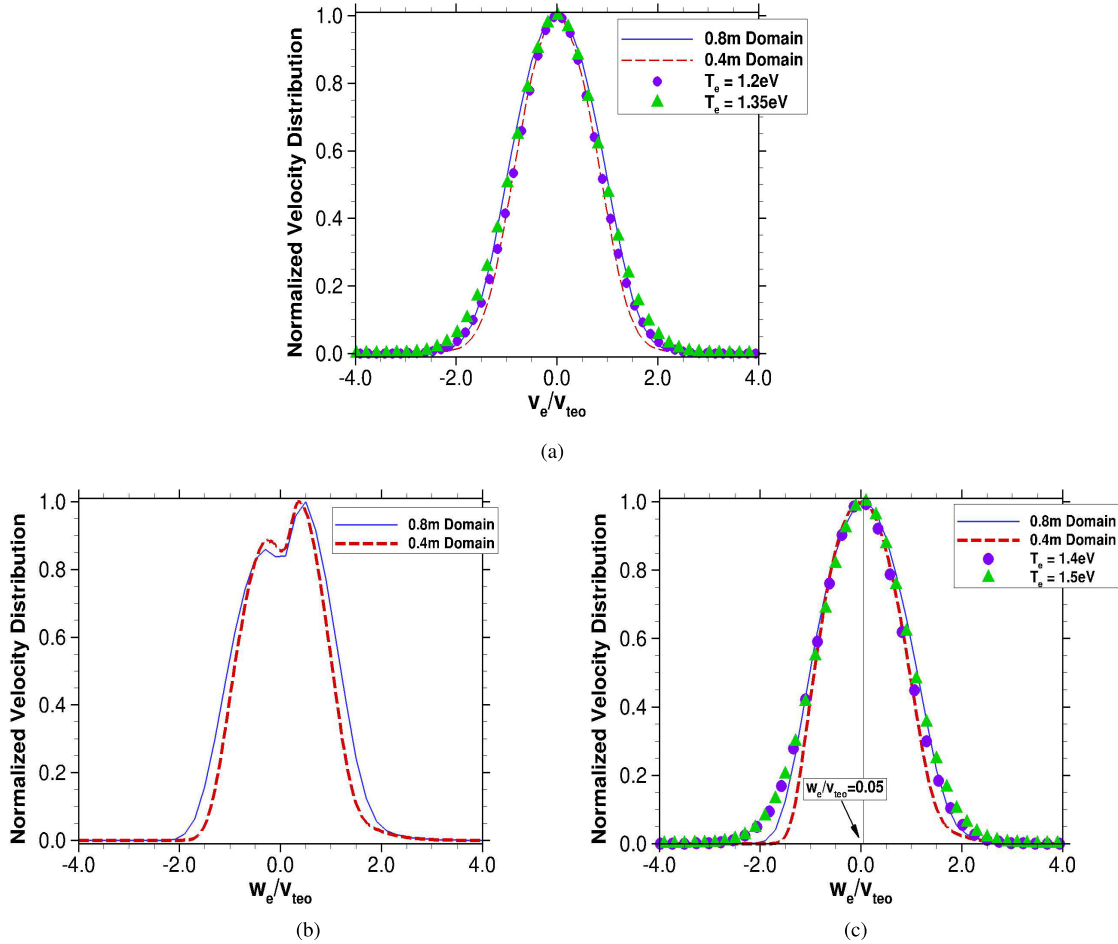


Fig. 11. Comparison of y - and z -EVDF at $z = 0.01$ and 0.2 m obtained from the 0.4 - and 0.8 -m colocated simulations. (a) y -EVDF at $z = 0.01$ m. (b) z -EVDF at $z = 0.01$ m. (c) z -EVDF at $z = 0.2$ m.

higher in the 0.8 -m simulation compared to the 0.4 -m case, which is consistent with the lower potential observed in the former case. Note that a potential difference of 0.38 V in the core region results in a thermal energy difference of 0.15 eV. This is because the electrons are sensitive to the small changes in the potential gradient on account of their lower mass, whereas the heavier ion species are not affected by small changes in the potential gradient.

One of the main advantages of using the CCE BC is improvement in computational efficiency obtained by performing simulations on a smaller domain, such that the near-field potential and its gradient agree with those obtained from a much larger domain size. The 0.4 -m simulation required 54 min to simulate 2000 timesteps at the steady state with 130 million charged particles and 2.23 million octree cells using 32 -T K20 GPUs. In contrast, the 0.8 -m simulation required 3.5 h to perform 2000 timesteps at the steady state with 262 million charged particles and 7.6 million octree cells using 32 -T K20 GPUs. Thus, the 0.4 -m domain is four times faster while predicting the electric potential with A reasonable agreement, both in the core as well as outside the plume region.

B. Shifted Case

In real ion thrusters, the external neutralizer is separated from the ion source, unlike the colocated configuration typically assumed in PIC simulations. In this section, we apply the CCE BC for the separated electron–ion configuration, shown in Fig. 1(b), and study the convergence of the electric potential as well as EVDF by systematically increasing the domain size from $(0.8 \times 0.8 \times 0.4)$ to $(0.8 \times 0.8 \times 0.8)$, and $(1.0 \times 1.0 \times 1.0)$ m. To study the effect of assuming quasi-neutrality and constant electron temperature, an additional simulation is performed on a $(0.8 \times 0.8 \times 0.8)$ m domain with a single ion source, assuming the Boltzmann relation to estimate the electric potential and the self-consistent flow-field. Note that since electrons are not explicitly modeled in the Boltzmann relation simulation, the shift in the electron source cannot be simulated. The electric potential, ϕ , in the Boltzmann simulation is computed as

$$\phi = \phi_o + \frac{k_b T_e}{e} \ln \left(\frac{n_e}{n_o} \right) \quad (4)$$

where ϕ_o is the reference potential, k_b is the Boltzmann constant, n_e is the the electron number density, which is equal

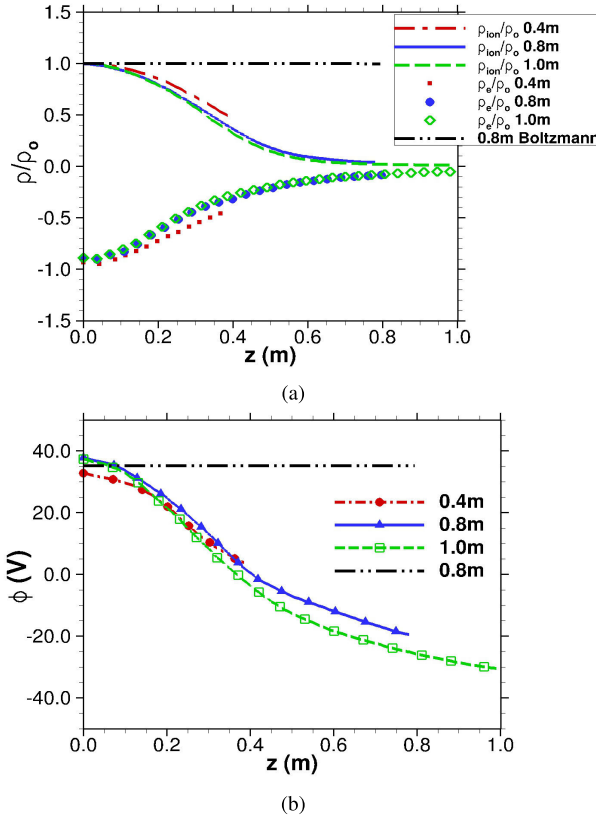


Fig. 12. Comparison of the charge density and the electric potential along the plume center-line obtained from the fully kinetic 0.4-, 0.8-, and 1.0-m domain simulations for the shifted configuration as well as the Boltzmann relation. (a) Ion and electron charge densities normalized by $\rho_o = e \cdot n_{eo}$. (b) Electric potential.

to the ion number density n_i due to quasi-neutrality, and $n_o = 1 \times 10^{13}/\text{m}^3$ is the reference electron number density similar to the fully kinetic cases. A reference potential of $\phi_o = 38$ V is set based on the potential obtained near the plume source from the fully kinetic simulation. All simulations were determined to have reached a steady state, if the instantaneous electric potential and EVDF at different time instants agreed within 2%. Macroparameters are sampled from $t\omega_{peo} = 10,000$, i.e., after 200 000 timesteps for 50 000 timesteps after the electric field reached a steady state. The variation of the total number of ions and electrons as a function of time is shown in Fig. 19 in Appendix C.

A comparison of the normalized, steady-state ion and electron charge density variations along the plume center-line obtained from the 0.4-, 0.8-, and 1.0-m fully kinetic PIC and the 0.8-m Boltzmann simulation is shown in Fig. 12(a). Unlike the constant ρ_i/ρ_o along the plume center-line obtained for the colocated simulation in Fig. 9(b), the normalized ion charge density decreases from unity to a value of 0.4, 0.1, and 0.05 at $z = 0.4, 0.8$, and 1.0 m downstream from the ion source, respectively, as shown in Fig. 12(a). In contrast, the Boltzmann solution predicts a constant ion charge density along the plume center-line, qualitatively similar to the colocated case shown in Fig. 9(b). This difference in the charge density variation obtained from the fully kinetic and Boltzmann simulations highlights that the latter may not be applicable to perform

neutralization simulations with separated electron-ion configurations due to the inability of these methods to resolve the electron bouncing mechanism [24] observed in these simulations. For the separated electron-ion configuration, as the electrons bounce radially with high cross-stream velocities [24], they spend very little residence time within the Plume, and as a result, only few electrons are trapped. This inefficiency in neutralization of the ion plume by a separate electron source causes the plume to expand more than that observed for the colocated electron-ion plume, as indicated by the decrease in the ion and electron charge densities shown in Fig. 12(a).

For the fully kinetic simulations using CCE BC, even though the electron source in the fully kinetic simulation is separated from the ion source, the electron charge density along the ion plume center-line is almost equal in magnitude to the ion charge density. This equivalence of the charge densities at the steady state indicates that the ion beam electrostatically traps electrons within the plume to neutralize the charge within the plume. The 0.4-m domain shows a 5%–10% higher ion and electron charge densities downstream of $z > 0.2$ m compared to the 0.8- and 1.0-m domain simulations. However, the excellent agreement of the charge density variation along the plume center-line obtained from the 0.8- and 1.0-m simulations suggests that the flow-field will converge only for a domain size equal to or larger than 0.8 m in all three directions for the shifted electron source configuration.

The variation of the steady-state electric potential along the plume center-line obtained from the 0.4-, 0.8-, and 1.0-m fully PIC and 0.8-m Boltzmann simulations is shown in Fig. 12(b). The potential obtained from the Boltzmann relation is constant along the plume center-line consistent with the constant ion charge density variation, qualitatively similar to the potential variation obtained for the colocated case in Fig. 9(b). On the contrary, the potential obtained from the fully PIC simulations decreases from the source to the $z = z_{\max}$ boundary along the plume center-line. This difference supports the previous conclusion that the quasi-neutrality assumption breaks down for a plume with a shifted electron source configuration due to the low residence time of electrons that bounce radially due to the electrostatic coupling induced by the separation of ion and electron sources. Comparing fully kinetic PIC results, it can be observed that the potential obtained from the 0.4-m simulation is 6 V lower at the ion source, $z = 0.0$, than that obtained from the 0.8- and 1.0-m simulations. This lower potential is due to the higher (more negative) electron charge density obtained for the 0.4-m simulation downstream of $z > 0.2$ m, shown previously in Fig. 12(a).

To investigate the cause of the difference in the electron charge density variation, the average electron energy of the 0.4-, 0.8-, and 1.0-m simulations, which is used as a criterion for electron reflection, were compared and found to agree within 2%. However, the average number of electrons that was reflected from the $z = z_{\max}$ boundary using this energy criterion was approximately 9900, 8800, and 8500 for the 0.4-, 0.8-, and 1.0-m simulations, respectively. This difference in the number of reflected electrons is because the electron charge density at $z = 0.4$ m is $0.5\rho_o$, while at $z = 0.8$ and 1.0 m, the charge density decreases to $0.1\rho_o$. The convergence

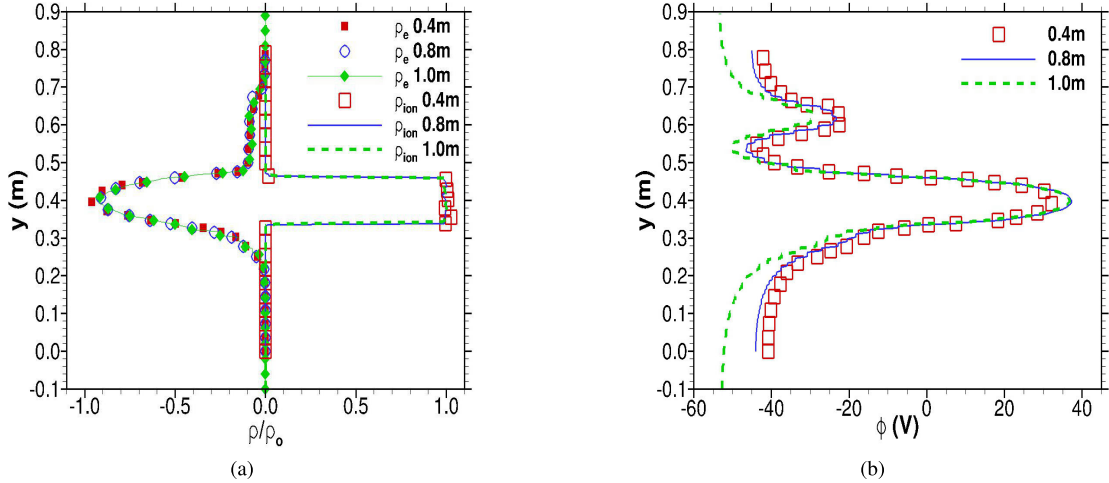


Fig. 13. Comparison of charge densities and electric potential perpendicular to the plume-axis obtained from the 0.4-, 0.8-, and 1.0-m simulations for the shifted electron source configuration. (a) Ion and electron charge densities normalized by ρ at $z = 0.01$ m. (b) Electron potential at $z = 0.01$ m.

of 0.8- and 1.0-m simulations suggests that the distance of the z domain boundary for the shifted electron source configuration must be such that it can accommodate the plume until the charge density drops below $0.2\rho_0$, i.e., by an order of magnitude. It should be noted that the same criterion is not required to determine the maximum domain size for the colocated case since the electron dynamics for the shifted source configuration involves more complex electrostatic bouncing and trapping mechanisms in both the y - and z -directions, unlike the colocated case where electrons undergo trapping mainly in the z -direction to collectively travel with the ion beam.

Even though the near-source potential from the 0.8- and 1.0-m simulations agree well; for $z > 0.2$ m, the potential from the 0.8-m case is 2 to 5 V higher than that obtained from the 1.0-m simulation. This difference in the electric potential, despite the agreement in the charge density, is due to the statistical noise on the order of $(\sqrt{N_e})^{-1}$, where N_e is the number of electrons per cell. There are more than 100 particles per cell upstream of $z = 0.4$ m; however, downstream of this location, the number of particles per cell decreased to 30 because the octree cells sub-divide to satisfy the local Debye length criterion. Therefore, the statistical noise due to the number of particles per cell is higher downstream of $z > 0.4$ m which, in turn, causes a larger deviation of 5 V in potential.

To compare the effect of the domain size on the plume expansion width, the charge density and the electric potential are extracted along lines perpendicular to the beam propagation direction, at $z = 0.01$ and 0.2 m in the center yz plane. The variation of the normalized ion and electron charge densities at $z = 0.01$ m along the y -direction obtained from the 0.4-, 0.8-, and 1.0-m simulations is compared in Fig. 13(a). It should be noted that the domain size in the cross-stream direction is 0.8 m for both the 0.4- and 0.8-m simulations. The electron charge densities from the 0.8- and 1.0-m simulations agree well, while the 0.4-m simulation has 2% higher electron charge density within the plume and agrees well with the

larger domain simulations outside the plume core region. The normalized ion charge densities from the three simulations agree within 1%, suggesting that the domain size does not affect the variation in the ion charge density. Due to the shift in the electron source, the variation profiles of the electron and ion charge densities are dissimilar in shape. Because the ions are initialized as a collimated beam with high beam velocity and low thermal velocity, they have a “top-hat” profile, while the thermal electrons that are attracted toward the beam display a gradual profile with a single peak at $z = 0.01$ m. In addition, the electron density variation is not symmetric about the plume center at $y = 0.4$ m.

As a result of the asymmetry in the electron charge density variation shown in Fig. 13(a), the electric potential variation presented in Fig. 13(b) is not symmetric along the y -axis. The potential is maximum at the plume center and reaches the local minima at $y = 0.525$ m, which is aligned with the location of the electron source. Compared to the 0.8- and 1.0-m simulations, the peak electric potential at the plume-center for the 0.4-m simulation is less by 6 V. However, this difference in the potential range of -53 – 38 V is approximately 6.5%, which may be considered an acceptable statistical variation based on the differences in domain size. Furthermore, away from the plume center, the 0.4- and 0.8-m simulations show a good agreement with a maximum difference of 2 V near the cross-stream boundaries at $y = 0$ and 0.8 m. As mentioned for the colocated case, the difference in the potential at the cross-stream boundaries, in-spite of the good agreement in the charge densities, is due to the statistical noise in the instantaneous number of particles that crosses the boundary, which is used to compute the non-homogeneous electric field. However, it should be noted that this difference in the electric potential at the cross-stream boundary does not affect the potential in the core region of the plume, as observed from the agreement between the 0.8- and 1.0-m cases at the plume core.

The effects of the separated electron–ion configuration, CCE BC, and domain size, on the electron kinetics are studied

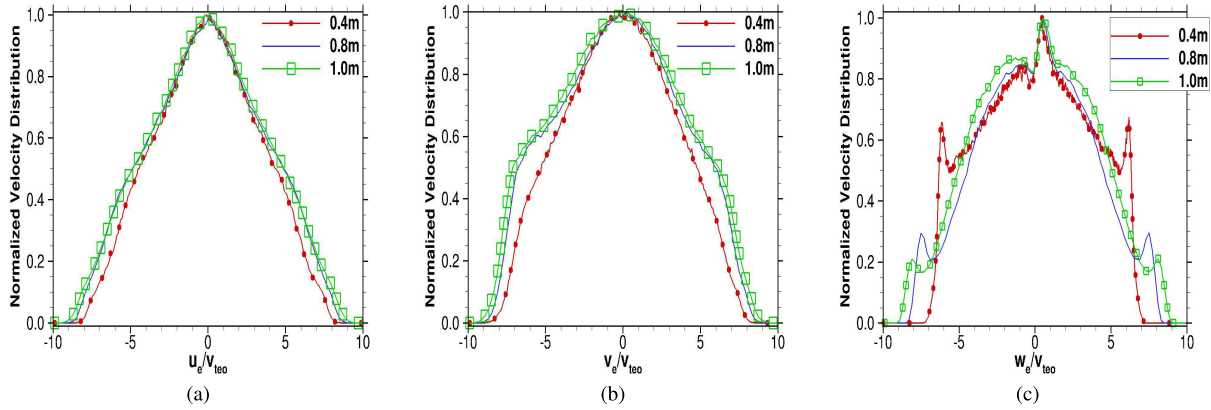


Fig. 14. Comparison of (a) x -, (b) y -, and (c) z -EVDFs at $z = 0.01$ m obtained from the 0.4-, 0.8-, and 1.0-m shifted electrons source simulations.

by sampling the steady-state x -, y -, and z -EVDFs within a radius of 0.05 m from the plume center-line at $z = 0.01$ and 0.2 m, respectively. The comparison of the x -, y -, z -EVDFs obtained near the ion source at $z = 0.01$ m from the 0.4-, 0.8-, and 1.0-m simulations is shown in Fig. 14(a)–(c), respectively. Unlike the symmetry in the cross-stream EVDFs obtained for the colocated case, the x - and y -EVDFs are not equal for the shifted configuration, and more importantly, the EVDFs are non-Maxwellian. For the x - and y -EVDFs shown in Fig. 14(a) and (b), the 0.8- and 1.0-m simulations show converged solutions, but the 0.4-m simulation shows a comparatively lower thermal spread. There are fewer energetic electrons compared to 0.8- and 1.0-m cases, and as a result, more electrons satisfy the energy criterion for reflection, which further increases the electron charge density and decreases the potential at the source, as previously observed in Fig. 12(a) and (b), respectively. The electrons emitted from the shifted source are first attracted toward the plume with a negative y -velocity. However, due to the high velocity, these electrons overshoot the radial edge of the plume leaving the plume with a positive charge. The positively charged plume then decelerates these electrons causing them to reverse the direction and flow toward the plume with a positive y -velocity. This trapping mechanism in the y -direction is indicated by the small secondary “bumps” in the y -EVDF at $w_e/v_{\text{teo}} = \pm 6$, obtained from the 0.8- and 1.0-m simulations at $z = 0.01$ m, shown in Fig. 14(b).

Unlike the single-peak distributions for the x - and y -EVDFs, the z -EVDF shown in Fig. 14(c) has two additional secondary peaks which are equidistant from the $w_e/v_{\text{teo}} = 0$ and of equal probability. These peaks are not physical and are attributed to the specular reflection performed at the z_{max} boundary to maintain the total charge in the domain for the CCE BC. The effect of this reflection on the EVDF is significant if the z_{max} boundary is closer to the ion source, as indicated by the higher secondary peaks obtained from the 0.4-m simulations compared to those of the 0.8- and 1.0-m simulations. However, in-spite of the proximity of the z_{max} boundary, the 0.4-m simulation captures the location of the central peak at $w_e/v_{\text{teo}} = 0.5$ similar to the 0.8- and 1.0-m simulations, displaying convergence for the profile of

the z -EVDF. Note that the same peak location at $w_e/v_{\text{teo}} = 0.5$ is also observed in Fig. 11(b) for the colocated z -EVDF sampled near the source at $z = 0.01$ m, indicating that the electrons emitted from the shifted source with high thermal velocity are electrostatically trapped near the ion source.

Notwithstanding these numerical effects of the CCE BC on the z -EVDF, macroparameters, such as the electric potential and charge density variation, exhibit convergence for the 0.8-m simulation, and since ions are not reflected at the boundary, no such secondary peaks are observed for the high-velocity beam ions. The computational speed-up of using a smaller domain size is analyzed by comparing the performance on the same supercomputer (Bluewaters with TeslaK20 GPUs) at the steady-state. The 0.4-m simulation required 30 min using 32 GPUs (i.e., 16 GPU hours) for every 2000 timesteps with 51.5 million particles and 0.6 million leaf nodes. For every 2000 timesteps at the steady-state, the 0.8- and 1.0-m simulations required 65 and 110 min each using 64 GPUs (i.e., 69 and 117 GPU hours), with 100 and 124.2 million particles and 2.47 and 2.65 million leaf nodes, respectively. The 0.8-m simulation is 1.7 times faster than the 1.0-m simulation. The 0.4-m simulation is 4.3 and 7.3 times faster than the 0.8- and 1.0-m simulations, respectively; however it predicts a 6-V difference in the electric potential. Note that this difference can be neglected, given that it leads to only 6.5% relative difference when normalized by the total potential ranging from -52 to 40 V, i.e., 92 V. Additional fully kinetic simulations were also performed to study the effect of the separation distance between the ion and electron sources, by increasing the separation distance between the ion and electron sources. On account of the higher separation distance, the electrons do not neutralize the plume efficiently, resulting in more positive potential for the plume. This increase in the plume potential increases the radial electric field, and as a result increases the thermal spread of the non-Maxwellian electron velocity distributions. Details of this study are discussed in Appendix D.

V. CONCLUSION

In this article, we present a new, general, self-consistent, open BC for the electron particles and the electric field which was developed to perform steady-state simulations of

ion thruster plasma plumes. The traditional outflow treatment for the particles and the homogeneous Neumann boundary employed for the electric field to model the open boundary cause the electrons initially trapped within the plume to rapidly exit the domain as the ion beam approaches the boundary. The newly developed CCE BC corrects this non-physical loss of electrons by reflecting electrons at the boundary to maintain the total baseline charge in the domain. This approach generated a stable, steady-state plume using three-dimensional octree-based fully kinetic simulations for colocated as well as separated ion and electron configurations, which to the best of our knowledge has not been done before.

Domain-independence studies were performed to study the sensitivity of the computed macroparameters, charge density, electric potential, and electron velocity distributions to changes in the location of the domain boundaries. For the colocated case, the charge density variation obtained from the simulation performed on a $(0.4 \times 0.4 \times 0.4)$ m domain showed a good agreement with that from the $(0.8 \times 0.8 \times 0.8)$ m domain. The electric potential from the smaller 0.4-m domain is in agreement with that of the 0.8-m simulation with a tolerance of 0.4 V inside the core of the plume and 2.4 V outside of the plume, which is acceptable given the statistical fluctuations inherent to particle-based methods. The EVDFs obtained from both the domain sizes indicated electrostatic trapping, where electrons collectively travel with the ion beam in the z -direction and anisotropic thermal distributions. Furthermore, the simulation using the 0.4-m domain required four times less computational time compared to the 0.8-m case, while producing results with reasonable accuracy.

The effect of the boundary location on the electron kinetics is more significant for the shifted electron configuration due to the more complex electron trapping mechanism caused by the separation of electron-ion sources. Comparing the fully kinetic simulations for the shifted electron configuration with the Boltzmann relation, it can be concluded that the latter is not valid to model plumes with an external neutralizer since the plume core is not strictly quasi-neutral and a constant electron temperature is an inaccurate representation of the evident non-Maxwellian EVDFs. Convergence in the electric potential along the plume center-line, obtained from the 0.8- and 1.0-m fully kinetic PIC simulations with the CCE BC, indicated that the streamwise boundary must be located at a distance downstream from the source, such that it can accommodate the plume until the initial charge density decreases by an order of magnitude. Unlike the colocated case, the EVDF obtained from the shifted source simulations was non-Maxwellian with unequal distributions in each direction. The electron reflection performed at the streamwise boundary, $z = z_{\max}$, to maintain the total baseline charge, causes the z -EVDF to have secondary peaks for the shifted source configuration. However, the secondary peaks do not significantly affect the charge density and electric potential variation.

It should be noted that the inefficiency of the neutralization and high potential difference between the plume and the surrounding region observed for the collisionless simulations of the separated ion-electron source configuration performed in this article are not observed in some ground-based ion

thruster experiments [38]. We attribute this difference to the small but finite background pressure present in ground-based facilities which impact the charge-exchange process and significantly affect the plume characteristics [39]. Detailed studies are required where the simulation set-up is similar to the ground-based facilities and space environment to understand the influence of the background pressure on ground-based experiments. Regardless, the proposed BC is applicable to such realistic simulations and will be considered in the future work. The PIC-DSMC collisions to include the crucial charge-exchange collisions will also be performed in the future. This open boundary construct may also be used to perform fully kinetic simulations of hall thruster plumes or astrophysical jets that require a free boundary.

APPENDIX A

INPUT PARAMETERS

The input parameters are given in Tables III and IV.

APPENDIX B

ANALYSIS OF REFLECTION AND INFLUX BCs

Reflection BC

From the outflow and buffer BC discussed in Sections III-A and III-B, respectively, it is understood that the negative half of the Maxwellian EVDF is compromised due to the local charge imbalance. This suggests that electrons should be reflected at the streamwise domain boundary ($z = z_{\max}$) to prevent them from exiting the domain, in a manner that prevents the loss of trapped electrons, thereby maintaining the expected z -EVDF for the colocated plume. In this approach, the number of ions and electrons leaving the $z = 0.4$ -m boundary every timestep is computed after the ion beam-front crosses the streamwise domain boundary. If the number of electrons exiting the domain is higher than the number of exiting ions, electrons with kinetic energy less than the energy corresponding to the inlet electron temperature (2 eV) are specularly reflected from the $z = z_{\max}$ boundary to counter-balance the loss of trapped electrons. The electrons that have energy higher than 2 eV are allowed to exit the domain since they have enough energy to escape the attractive electrostatic force exerted by the ion beam. Similar to the previously discussed BC, the buffer BC is implemented at the cross-stream boundaries $x_{\min}, x_{\max}, y_{\min}, y_{\max}$ and the particles crossing the $z = 0$ inlet plane are deleted from the computational domain. The electric field BC at all the boundaries is the same as that described for the buffer BC in the previous section.

The stable instantaneous ion and electron charge density distributions at $t\omega_{peo} = 2300$ and 3800, shown in Fig. 15(a) and (b), demonstrate that the reflection BC prevents the numerical loss of trapped electrons at the boundary better than the previously discussed outflow and buffer BCs. As a result, even though the ion beam-front crosses the computational domain, the local charge at the boundary is balanced, and electrons are not non-physically removed from the domain. However, the quasi-neutral electric potential at $t\omega_{peo} = 2.300$ observed in Fig. 15(c) is not maintained at $t\omega_{peo} = 3.800$, as shown in Fig. 15(d) and is not in agreement

TABLE III
INPUT PARAMETERS AND STEADY-STATE VALUES FOR THE FULLY KINETIC PIC SIMULATIONS
OF THE COLOCATED TEST CASES DISCUSSED IN SECTION IV-A

Input parameters	0.4 m simulation	0.8 m simulation
Domain Size (m)	0.4×0.4×0.4	0.8×0.8×0.8
No. of timesteps prior to sampling	100,000	120,000
No. of samples	80,000	80,000
Average electron energy (J)	5.9×10^{-18}	8.619×10^{-18}
Total charge in the domain ($(N_i - N_e)/e$)	-168876	-212010
No. of particles (M)	130	262
Total no. of leaf nodes (M)	2.23	7.6
Min. leaf node size (m) **	1.56×10^{-3}	1.56×10^{-3}
Max. leaf node size (m) **	0.025	0.05
Simulation run time for 2,000 timesteps ** (hr)	0.9	3.5
Number of Tesla K20 GPUs used	32	32

Initial electron number density ($n_{eo} = 1 \times 10^{13} \text{ m}^{-3}$); Initial electron temperature $T_{eo}=2 \text{ eV}$

Initial electron plasma frequency ($\omega_{peo}=1.7 \times 10^8 \text{ rad/s}$)

Initial electron thermal velocity, $v_{teo}=592,892 \text{ m/s}$

Initial ion number density = $4 \times 10^{13} \text{ m}^{-3}$, Ion beam velocity $v_{ibeam}=30,000 \text{ m/s}$

‡ SS = Steady-state macroparameters

TABLE IV
INPUT PARAMETERS AND STEADY-STATE VALUES FOR THE FULLY KINETIC PIC SIMULATIONS
OF THE COLOCATED TEST CASES DISCUSSED IN SECTION IV-B

Input parameters	0.4 m simulation	0.8 m simulation	1.0 m simulation
Domain Size (m)	0.8×0.8×0.4	0.8×0.8×0.8	1.0×1.0×1.0
No. of timesteps prior to sampling	200,000	200,000	200,000
No. of samples	50,000	50,000	50,000
Average electron energy (J)	3.5×10^{-18}	3.2×10^{-18}	3.1×10^{-18}
Total charge in the domain ($(N_i - N_e)/e$)	-2,568,057	-2,732,648	-2,995,666
No. of particles (M)	51.5	100	124.2
Total no. of leaf nodes (M)	0.6	2.47	2.65
Min. leaf node size (mm) **	3.12×10^{-3}	3.12×10^{-3}	3.12×10^{-3}
Max. leaf node size (mm) **	0.025	0.025	0.025
Simulation run time for 2,000 timesteps ** (hr)	0.5	1.08	1.83
Number of Tesla K20 GPUs	32	64	64

Initial electron number density ($n_{eo} = 1 \times 10^{13} \text{ m}^{-3}$); Initial electron temperature $T_{eo}=2 \text{ eV}$

Initial electron plasma frequency ($\omega_{peo}=1.7 \times 10^8 \text{ rad/s}$)

Initial electron thermal velocity, $v_{teo}=592,892 \text{ m/s}$

Initial ion number density = $1 \times 10^{13} \text{ m}^{-3}$, Ion beam velocity $v_{ibeam}=30,000 \text{ m/s}$

‡ SS = Steady-state macroparameters

with the quasi-neutral result obtained for the colocated plume in our previous work [24] when the plume was terminated before the beam-front reached the boundary. The decrease in the potential that occurs indicates an increase in the density of trapped electrons, which may be due to the incorrect assumption that the thermal energy of the reflected electrons should be close to the inlet temperature of 2 eV. This assumption is incorrect because the z -EVDF at the beam-front, when it is not influenced by the boundary, is close to 1.5 eV as shown in Fig. 3(a) and 6 due to plume expansion. Since a higher thermal energy criterion for electron reflection was

assumed, the electron charge density increased compared to the ion charge density, which in turn, caused the potential to decrease to -7 V at $z = 0.2 \text{ m}$. It should be noted that even if an accurate thermal energy criterion based on accurate temperature was used for electron reflection, the assumption that the z -EVDF would be Maxwellian is not sufficiently general to extend to the shifted source case, which showed a non-Maxwellian EVDF [24]. Therefore, even though the reflection BC results in a stable plume, a temperature-based criterion for electron reflection to ensure an equal outflux of ions and electrons is not a sufficiently general BC to obtain

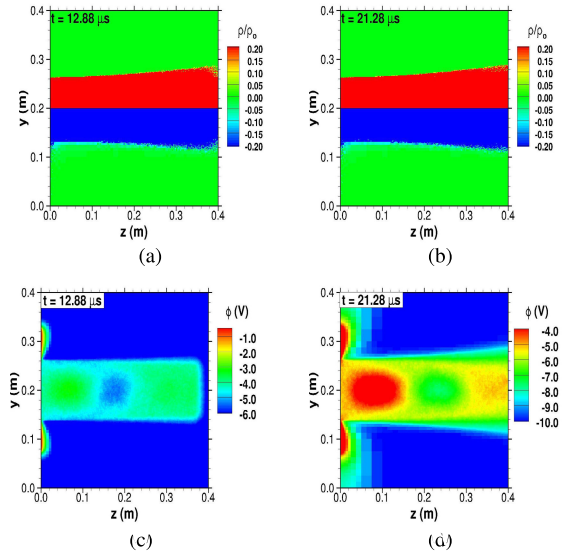


Fig. 15. Evolution of charge distribution and electric potential obtained using the reflection BC. (a) Ion and electron charge distributions at $t\omega_{\text{peo}} = 2300$. (b) Ion and electron charge distributions at $t\omega_{\text{peo}} = 3800$. (c) Electric potential at $t\omega_{\text{peo}} = 2300$. (d) Electric potential at $t\omega_{\text{peo}} = 3800$.

accurate steady-state plume characteristics for real ion thruster configurations.

Influx BC

The major drawback of the outflow, buffer, and reflection BC is their inability to conserve the total charge when the beam-front crosses the domain boundary. The influx BC explicitly conserves the total charge in the domain by controlling the electron influx at the electron source. That is, when the first ion particle crosses the region $4\lambda_d$ upstream of the domain boundary, the total charge in the domain, given by $Q = q(N_i - N_e)$ is computed, where Q is the total baseline charge, q is the elementary charge, and N_i and N_e are the total number of ions and electrons in the domain, respectively. At all the subsequent timesteps, the instantaneous total charge Q^k at the k th timestep is re-computed and if the difference between the instantaneous and baseline total charges ($Q^k - Q$) > 0 , then the number of electrons required to maintain Q is computed. These additional electrons are introduced from the electron source with the thermal energy equal to the initial inlet temperature of 2 eV. The electric field BCs are the same as that used for the buffer BC discussed in Section III-B and summarized in Table I.

Fig. 16(a) and (b) shows the stable ion and electron charge distributions obtained using the influx BC at $t\omega_{\text{peo}} = 2.300$ and 3200, respectively. Since the core region of the plume (the region with charge density higher than $0.2\rho_0$) is quasi-neutral right before the ion beam-front crosses the domain, as shown in Fig. 16(c), and the total charge is conserved by introducing electrons at the inlet source, the plume continues to be quasi-neutral even after 900 $t\omega_{\text{peo}}$ time-periods from the instant the ion beam-front first crosses the boundary, as shown in Fig. 16(d). The influx BC thus resulted in a stable and quasi-neutral plume. However, on sampling the velocity

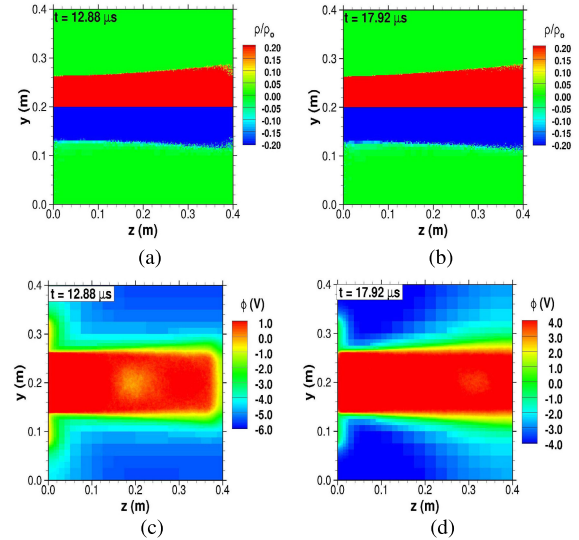


Fig. 16. Transient charge distribution and electric potential obtained using the influx BC along the yz plane extracted at the center of the domain. (a) Ion and electron charge distributions $t\omega_{\text{peo}} = 2300$, normalized by ρ_0 . (b) Ion and electron charge distributions $t\omega_{\text{peo}} = 3200$, normalized by ρ_0 . (c) Instantaneous electric potential at $t\omega_{\text{peo}} = 2300$. (d) Instantaneous electric potential at $t\omega_{\text{peo}} = 3200$.

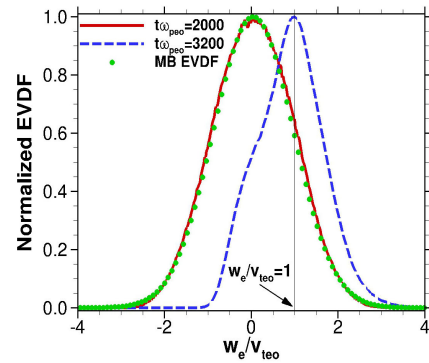


Fig. 17. Comparison of z -EVDF obtained using the influx BC at $t\omega_{\text{peo}} = 2300$ and 3200 with Maxwellian at $T_e = 1.4$ eV and $w_e = 30.000$ m/s.

distribution of electrons at $z = 0.2$ m, the z -EVDF is in agreement with a Maxwellian distribution at $T_e = 1.4$ eV and a bulk velocity of 30 000 m/s at $t\omega_{\text{peo}} = 2000$, but evolves to a non-Maxwellian distribution at $t\omega_{\text{peo}} = 3200$ with a peak normalized velocity of $w_e/v_{\text{teo}} = 1$, as shown in Fig. 17. This shift in the peak value of the z -EVDF from 0.05 to 1 is non-physical and is caused by the increased influx of electrons that were introduced at the source to conserve the total charge. Since the number density of electrons remained stable, as observed from Fig. 16(b), the increase in the electron flux, which is a function of the product of electron number density and bulk velocity, altered the average bulk velocity of electrons to allow for the additional electron influx, resulting in a kinetically incorrect result. The transition of the z -EVDF from Maxwellian at $t\omega_{\text{peo}} = 2000$ to non-Maxwellian at $t\omega_{\text{peo}} = 3200$, with a slight bulge at $w_e/v_{\text{teo}} = 0$ highlighted in Fig. 17 indicates the mixing of the previously trapped electrons with the newly introduced electrons from the source. Thus, introducing additional electrons from the source to

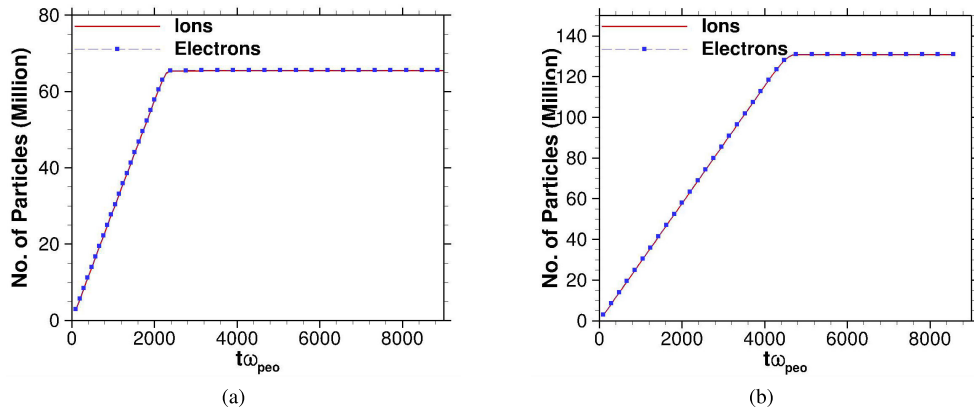


Fig. 18. Variation of the total number of charged computational particles in the domain with increase in the plasma time period for the colocated cases. (a) 0.4-m simulation. (b) 0.8-m simulation.

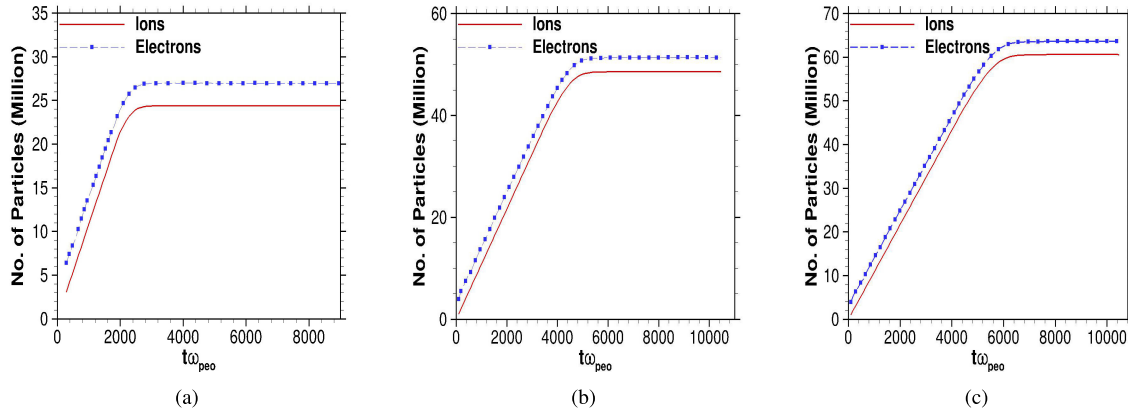


Fig. 19. Variation of the total number of charged computational particles in the domain with increase in the plasma time period for the shifted electron source cases. (a) 0.4-m simulation. (b) 0.8-m simulation. (c) 1.0-m simulation.

maintain the total charge density increases the electron flux at the source, which, in turn, leads to non-physical electron kinetics.

APPENDIX C DEMONSTRATION OF STEADY STATE FOR THE MESOTHERMAL CASES

The variation of the number of particles with time for the colocated 0.4- and 0.8-m simulations is shown in Fig. 18(a) and (b), respectively. It can be seen that the total number of ions and electrons in the domain reaches a constant value beyond $t\omega_{peo} > 2500$ and 5000 for the 0.4- and 0.8-m simulations, respectively. The variation of the number of particles with time for the shifted 0.4-, 0.8-, and 1.0-m simulations is shown in Fig. 19(a)–(c), respectively. It can be seen that the number of ion and electron particles become steady beyond $t\omega_{peo} > 3000$, 5000 and 7000 for the 0.4-, 0.8-, and 1.0-m simulations, respectively.

APPENDIX D EFFECT OF THE DISTANCE BETWEEN THE ION AND ELECTRON SOURCES ON THE PLUME AND ELECTRON KINETICS

To determine the effect of the electron source location on the plume dynamics and electron kinetics, the center of

the electron source is shifted by $2.5R$ from the ion source center, which was previously at a distance of $2R$ for the baseline electron source configuration shown in Fig. 1(b). Note that $R = 0.0625$ m is the radius of ion and electron sources. The $2.5R$ case is performed with a domain size of $(1.2 \times 1.2 \times 0.8)$ m, and is compared with the baseline $(0.8 \times 0.8 \times 0.8)$ m simulation discussed in the previous section.

The variation of the ion and electron charge densities along the plume center-line obtained from the $2.5R$ case and normalized by $\rho_o = e \cdot n_{eo}$ is compared with that from the baseline $2R$ case in Fig. 20(a). Even though electrons are initialized at the source with the same input parameters, the density of the electrons trapped by the ion plume is lower for the $2.5R$ case compared to the baseline $2R$ case. It should be noted that the electrons are initialized at the source with a stationary Maxwellian of $T_{eo} = 2$ eV and with no velocity bias toward the ion plume. Therefore, when the separation distance between the electron and ion sources is increased, more energetic thermal electrons are lost to the boundaries and fewer electrons are attracted toward the ion plume. Consistent with the large difference in the ion and electron charge densities seen for the $2.5R$ and $2R$ cases, the electric potential obtained from the $2.5R$ case is higher by 80 V near the ion source compared to the baseline, as shown

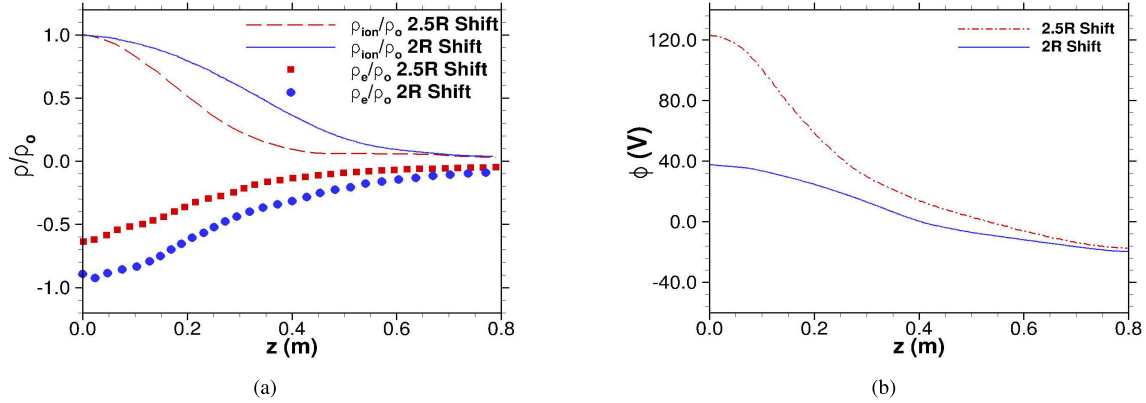


Fig. 20. Comparison of charge density and electric potential along the plume center-line obtained from the $2.5R$ - and $2R$ -shifted electron source simulations. (a) Ion and electron charge densities normalized by $\rho_o = e \cdot n_{eo}$. (b) Electric potential.

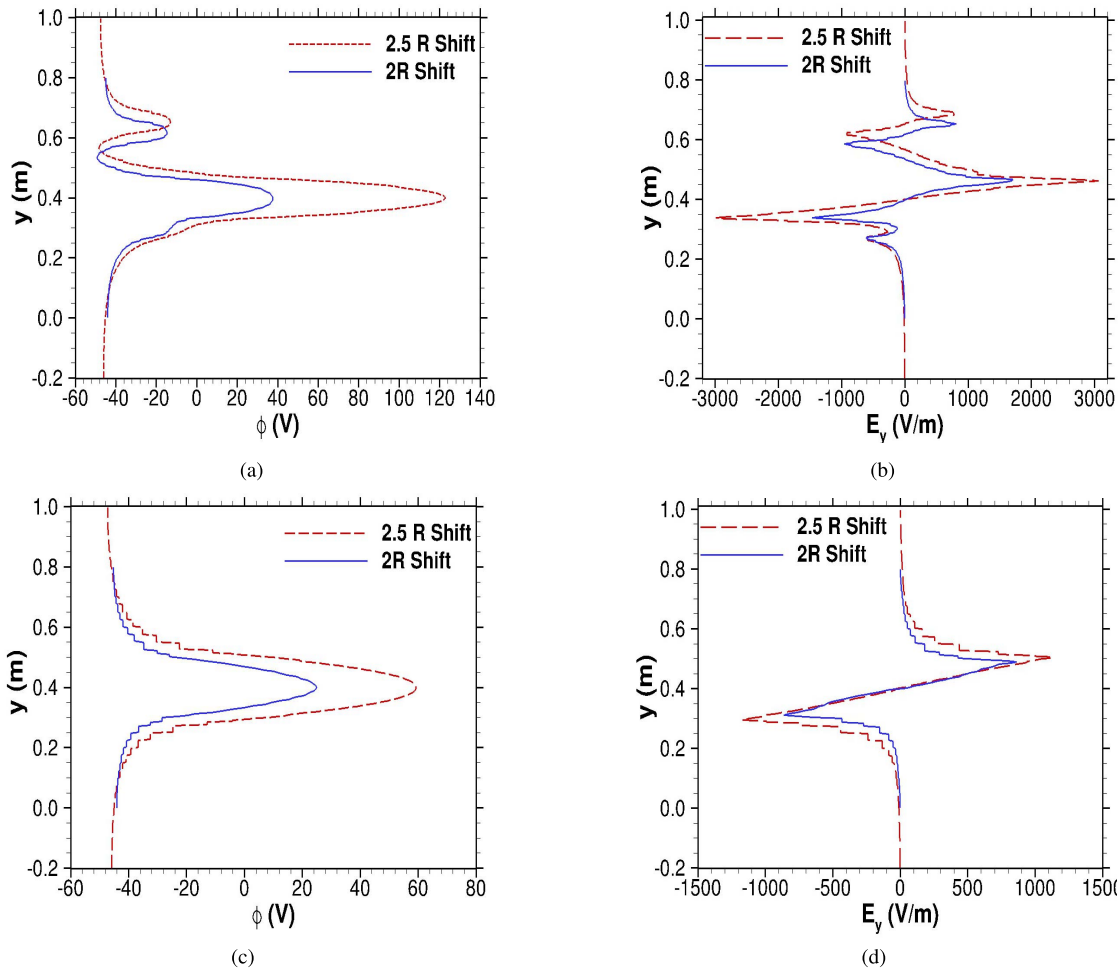


Fig. 21. Comparison of the electric potential and the E_y electric field along the y -direction at $z = 0.01$ and 0.2 m obtained from the $2.5R$ and baseline $2R$ cases. (a) Electric potential at $z = 0.01$ m. (b) y -component of the electric field, E_y , at $z = 0.01$ m. (c) Electric potential at $z = 0.2$ m. (d) y -component of the electric field, E_y , at $z = 0.2$ m.

in Fig. 20(b). Due to reduction in the number of trapped electrons, the ions within the plume undergo repulsion in the radial direction, and consequently the ion charge density decreases more rapidly for the $2.5R$ case compared to that of the baseline. Similar to the ion charge density variation,

the electric potential obtained for the $2.5R$ case also decreases rapidly from $\phi = 120$ V at $z = 0$ to $\phi = 20$ V at $z = 0.4$ m, and finally decreases to zero close to $z = 0.6$ m where the ion and electron charge densities are equal in magnitude and opposite in charge. In contrast, the decrease in the potential

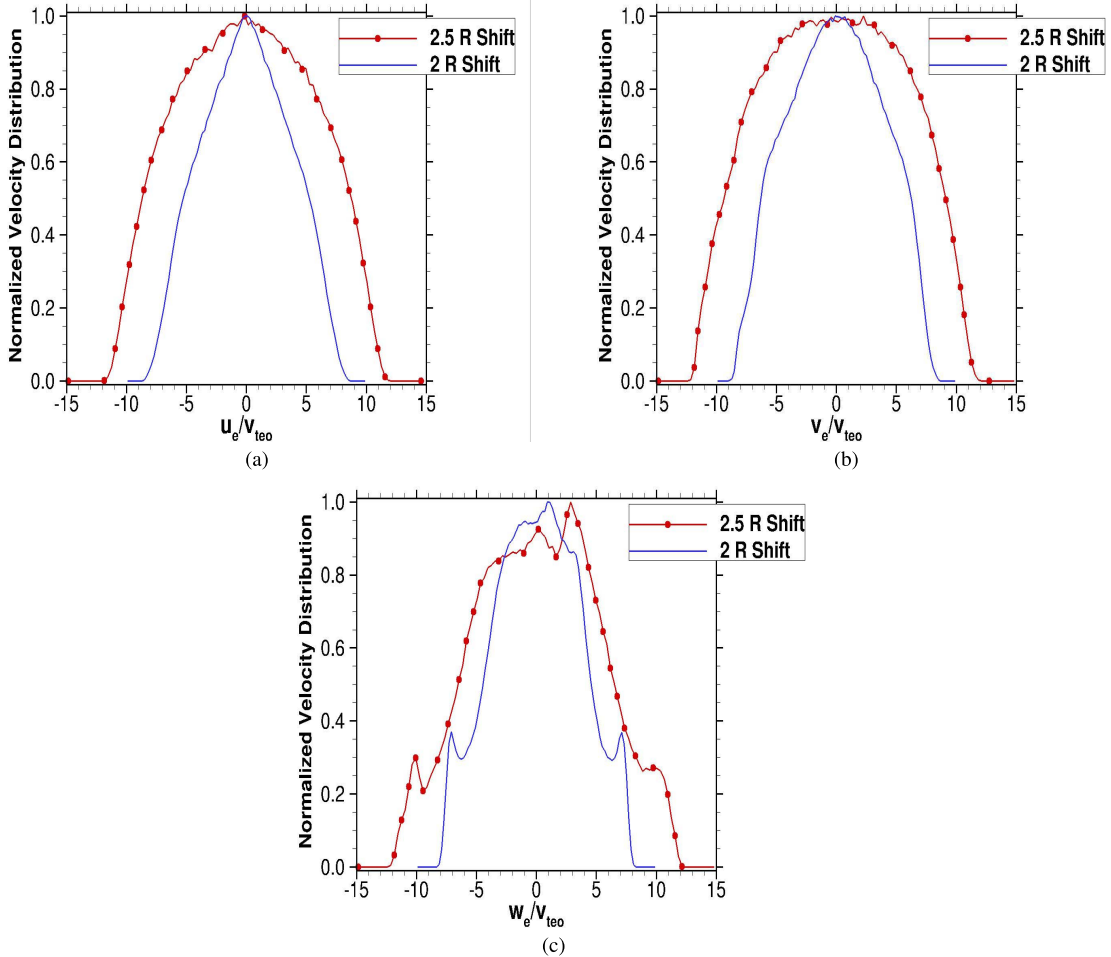


Fig. 22. Comparison of (a) x -, (b) y -, and (c) z -EVDFs obtained from shifted electron source cases with different separation distances from the ion source centers.

along the plume center-line is more gradual for the baseline case, as shown in Fig. 20(b).

The effect of the separation distance between the electron and ion sources on the cross-stream variation of electric potential and the electric field, E_y , is analyzed by extracting the steady-state results along lines perpendicular to the beam propagation direction, at $z = 0.01$ and 0.2 m. The variation of the steady-state electric potential along the y -direction at $z = 0.01$ m obtained from the $2.5R$ and baseline ($2R$) simulations are compared in Fig. 21(a). Since the electrons are initialized with the same number density, the potential of $\phi = -44$ V is the same at the location of the electron source centers, $y = 0.525$ and 0.556 m, for the baseline and $2.5R$ cases, respectively. However, because the electron charge density trapped in the ion plume is lower, the peak electric potential is higher for the $2.5R$ case compared to the $2R$ case. As a consequence of this higher electric potential, the gradient of the electric potential along the y -direction is higher for the $2.5R$ case, as observed from the comparison of the y -component of the electric field in Fig. 21(b). The peak E_y from the $2.5R$ case is two times higher than that obtained for the baseline case. As a result, the electrons emitted from the $2.5R$ source undergo higher acceleration toward the plume compared to the baseline case. Further downstream, at $z = 0.2$ m, the peak electron potential obtained

from the $2.5R$ case is 40 V higher than the baseline case potential, as shown in Fig. 21(c). Compared to the near-source region, the y -component of the electric field from the $2.5R$ simulation is lower downstream ($z = 0.2$ m); however, the peak E_y is still 270 V/m higher in magnitude compared to that obtained from the baseline case at the same location, as shown in Fig. 21(d).

To study the effect of the increase in the electric field on the electric kinetics, the x -, y -, and z -EVDFs sampled from both the simulations, at $z = 0.2$ m within a radius of 0.05 m about the plume center-line, are compared in Fig. 22(a)–(c), respectively. It can be seen that when the electron source center is shifted by $2.5R$, the x - and y -EVDFs shown in Fig. 22(a) and (b), respectively, still have single peaks similar to the baseline-shifted configuration; however, the electron energy is higher (wider thermal spread) for the $2.5R$ case compared to the baseline. This increase in the energy is a result of the higher electric field, E_y , shown in Fig. 21(b) and (d). The z -EVDF also has a larger thermal spread (width) compared to the baseline consistent with the higher electric field in the z -direction for the $2.5R$ case indicated by a comparatively rapid decrease in the electric potential, shown in Fig. 20(b). The z -EVDF obtained from the $2.5R$ case is slightly more noisy in the peak region compared to the $2R$ case, because the electron number density for the $2.5R$ case at $z = 0.2$ m is less

than that of the $2R$ case, as seen from Fig. 20(a), resulting in relatively fewer statistics. The secondary peaks caused due to the electron reflection at the z_{\max} boundary are also observed for the z -EVDF obtained from the $2.5R$ case. Since the average energy for the $2.5R$ case is higher, the secondary peaks are located at $w_e/v_{teo} = \pm 10$ for the $2.5R$ case, which is greater than the value of $w_e/v_{teo} = \pm 8$ for the baseline case. From this article, we find that when the electron source is shifted farther from the ion source, and if the electrons are initialized with a stationary unbiased Maxwellian, the plume neutralization is not efficient. The resulting increase in the electric field causes the electrons to undergo higher acceleration or deceleration, thereby increasing the kinetic energy of electrons.

ACKNOWLEDGMENT

The authors are grateful for the funding support provided by AFOST through the GRANT AF FA9550-16-1-0193. This research is part of the Blue Waters sustained-petascale computing project, which is supported by the National Science Foundation (awards OCI-0725070 and ACI-1238993) and the state of Illinois. Blue Waters is a joint effort of the University of Illinois at Urbana–Champaign and its National Center for Supercomputing Applications. The authors also acknowledge XSEDE for providing the computational resource on XStream.

REFERENCES

- [1] D. M. Goebel and I. Katz, *Fundamentals of Electric Propulsion: Ion and Hall Thrusters*, vol. 1. Hoboken, NJ, USA: Wiley, 2008.
- [2] H. Kuninaka and P. Molina-Morales, “Spacecraft charging due to lack of neutralization on ion thrusters,” *Acta Astronautica*, vol. 55, no. 1, pp. 27–38, Jul. 2004.
- [3] T. Hyakutake, M. Nishida, H. Kuninaka, and K. Toki, “DSMC-PIC analysis of a plume from MUSES-C ion engines,” *Trans. Jpn. Soc. Aeronaut. Space Sci.*, vol. 46, no. 151, pp. 24–30, 2003.
- [4] C. Birdsall, “Particle-in-cell charged-particle simulations, plus Monte Carlo collisions with neutral atoms, PIC-MCC,” *IEEE Trans. Plasma Sci.*, vol. 19, no. 2, pp. 65–85, Apr. 1991.
- [5] J. Deca, A. Divin, G. Lapenta, B. Lembège, S. Markidis, and M. Horányi, “Electromagnetic particle-in-cell simulations of the solar wind interaction with lunar magnetic anomalies,” *Phys. Rev. Lett.*, vol. 112, Apr. 2014, p. 151102.
- [6] T. D. Arber *et al.*, “Contemporary particle-in-cell approach to laser-plasma modelling,” *Plasma Phys. Control. Fusion*, vol. 57, no. 11, Nov. 2015, Art. no. 113001.
- [7] A. A. Philippov, A. Spitkovsky, and B. Cerutti, “*Ab initio* pulsar magnetosphere: Three-dimensional particle-in-cell simulations of oblique pulsars,” *Astrophys. J. Lett.*, vol. 801, no. 1, p. L19, Mar. 2015.
- [8] S. Choi and M. Kushner, “A particle-in-cell simulation of dust charging and shielding in low pressure glow discharges,” *IEEE Trans. Plasma Sci.*, vol. 22, no. 2, pp. 138–150, Apr. 1994.
- [9] G. Lapenta, “DEMOCRITUS: An adaptive particle in cell (PIC) code for object-plasma interactions,” *J. Comput. Phys.*, vol. 230, no. 12, pp. 4679–4695, Jun. 2011.
- [10] J. P. Boeuf, “Characteristics of a dusty nonthermal plasma from a particle-in-cell Monte Carlo simulation,” *Phys. Rev. A, Gen. Phys.*, vol. 46, no. 12, pp. 7910–7922, Jul. 2002.
- [11] I. D. Boyd and R. A. Dressler, “Far field modeling of the plasma plume of a Hall thruster,” *J. Appl. Phys.*, vol. 92, no. 4, pp. 1764–1774, Aug. 2002.
- [12] I. D. Boyd and J. T. Yim, “Modeling of the near field plume of a Hall thruster,” *J. Appl. Phys.*, vol. 95, no. 9, pp. 4575–4584, May 2004.
- [13] F. Taccogna, S. Longo, and M. Capitelli, “Particle-in-cell with Monte Carlo simulation of SPT-100 exhaust plumes,” *J. Spacecraft Rockets*, vol. 39, no. 3, pp. 409–419, May 2002.
- [14] R. I. S. Roy, D. E. Hastings, and N. A. Gastonis, “Ion-thruster plume modeling for backflow contamination,” *J. Spacecraft Rockets*, vol. 33, no. 4, pp. 525–534, Jul. 1996.
- [15] J. Wang, D. Brinza, and M. Young, “Three-dimensional particle simulations of ion propulsion plasma environment for deep space 1,” *J. Spacecraft Rockets*, vol. 38, no. 3, pp. 433–440, May 2001.
- [16] C. Cai, “Numerical studies on plasma plume flows from a cluster of electric propulsion devices,” *Aerospace Sci. Technol.*, vol. 41, pp. 134–143, Feb. 2015.
- [17] S. Cheng, M. Santi, M. Celik, M. Martinez-Sanchez, and J. Peraire, “Hybrid PIC-DSMC simulation of a Hall thruster plume on unstructured grids,” *Comput. Phys. Commun.*, vol. 164, nos. 1–3, pp. 73–79, 2004.
- [18] F. Taccogna, S. Longo, M. Capitelli, and R. Schneider, “Stationary plasma thruster simulation,” *Comput. Phys. Commun.*, vol. 164, nos. 1–3, pp. 160–170, Dec. 2004.
- [19] G. Lapenta, “Particle simulations of space weather,” *J. Comput. Phys.*, vol. 231, no. 3, pp. 795–821, Feb. 2012.
- [20] R. W. Hockney and J. W. Eastwood, *Computer Simulation Using Particles*. Boca Raton, FL, USA: CRC Press, 1988.
- [21] B. Korkut, Z. Li, and D. A. Levin, “3-D simulation of ion thruster plumes using Octree adaptive mesh refinement,” *IEEE Trans. Plasma Sci.*, vol. 43, no. 5, pp. 1706–1721, May 2015.
- [22] I. D. Boyd and M. W. Crofton, “Modeling the plasma plume of a hollow cathode,” *J. Appl. Phys.*, vol. 95, no. 7, pp. 3285–3296, Apr. 2004.
- [23] F. Cichocki, A. Domínguez-Vázquez, M. Merino, and E. Ahedo, “Hybrid 3D model for the interaction of plasma thruster plumes with nearby objects,” *Plasma Sources Sci. Technol.*, vol. 26, no. 12, 2017, Art. no. 125008.
- [24] R. Jambunathan and D. A. Levin, “CHAOS: An octree-based PIC-DSMC code for modeling of electron kinetic properties in a plasma plume using MPI-CUDA parallelization,” *J. Comput. Phys.*, vol. 373, pp. 571–604, Nov. 2018.
- [25] J. Wang, O. Chang, and Y. Cao, “Electron-ion coupling in mesothermal plasma beam emission: Full particle PIC simulations,” *IEEE Trans. Plasma Sci.*, vol. 40, no. 2, pp. 230–236, Feb. 2012.
- [26] L. Brieda and J. Wang, “Modelling ion thruster beam neutralization,” in *Proc. 41st AIAA/ASME/SAE/ASEE Joint Propuls. Conf. Exhibit*, 2005, p. 4045.
- [27] L. Brieda, “Development of the DRACO ES-PIC code and fullykinetic simulation of ion beam neutralization,” Ph.D. dissertation, Dept. Aerosp. Eng., Virginia Tech, Blacksburg, VA, USA, 2005.
- [28] Y. Hu and J. Wang, “Electron properties in collisionless mesothermal plasma expansion: Fully kinetic simulations,” *IEEE Trans. Plasma Sci.*, vol. 43, no. 9, pp. 2832–2838, Sep. 2015.
- [29] Y. Hu and J. Wang, “Fully kinetic simulations of collisionless, mesothermal plasma emission: Macroscopic plume structure and microscopic electron characteristics,” *Phys. Plasmas*, vol. 24, no. 3, Mar. 2017, Art. no. 033510.
- [30] R. J. Procassini, C. K. Birdsall, and E. C. Morse, “A fully kinetic, self-consistent particle simulation model of the collisionless plasma–sheath region,” *Phys. Fluids B, Plasma Phys.*, vol. 2, no. 12, pp. 3191–3205, Dec. 1990.
- [31] K.-U. Riemann, “The Bohm criterion and sheath formation,” *J. Phys. D: Appl. Phys.*, vol. 24, no. 4, pp. 493–518, Apr. 1991.
- [32] K. Hara, “Development of grid-based direct kinetic method and hybrid kinetic-continuum modeling of Hall thruster discharge plasmas,” Ph.D. dissertation, Dept. Aerosp. Eng., Univ. Michigan, MI, USA, 2015.
- [33] L. Brieda, “Model for steady-state fully kinetic ion beam neutralization studies,” *IEEE Trans. Plasma Sci.*, vol. 46, no. 3, pp. 556–562, Mar. 2018.
- [34] M. Li, M. Merino, E. Ahedo, and H. Tang, “On electron boundary conditions in PIC plasma thruster plume simulations,” *Plasma Sour. Sci. Technol.*, vol. 28, no. 3, Feb. 2019, Art. no. 034004.
- [35] R. Jambunathan, “CHAOS: A Multi-GPU PIC-DSMC solver for modeling gas plasma flows,” Ph.D. dissertation, Dept. Aerosp. Eng., Univ. Illinois Urbana-Champaign, Champaign, IL, USA, 2019.
- [36] A. Klimas, M. Hesse, and S. Zenitani, “Particle-in-cell simulation of collisionless reconnection with open outflow boundaries,” *Phys. Plasmas*, vol. 15, no. 8, Aug. 2008, Art. no. 082102.
- [37] C. K. Birdsall and A. B. Langdon, *Plasma Physics Via Computer Simulation*. Boca Raton, FL, USA: CRC Press, 2004.
- [38] J. Foster, G. Soulas, and M. Patterson, “Plume and discharge plasma measurements of an NSTAR-type ion thruster,” in *Proc. 36th AIAA/ASME/SAE/ASEE Joint Propuls. Conf. Exhibit*, Jul. 2000, p. 3812.
- [39] B. Korkut, D. A. Levin, and O. Tumuklu, “Simulations of ion thruster plumes in ground facilities using adaptive mesh refinement,” *J. Propuls. Power*, vol. 33, no. 3, pp. 681–696, May 2017.